

NON-LTE MODELS AND THEORETICAL SPECTRA OF ACCRETION DISKS IN ACTIVE GALACTIC NUCLEI. III. INTEGRATED SPECTRA FOR HYDROGEN-HELIUM DISKS

IVAN HUBENY

AURA/NOAO, NASA Goddard Space Flight Center, Code 681, Greenbelt, MD 20771

ERIC AGOL

Department of Physics and Astronomy, Johns Hopkins University, Baltimore, MD 21218

OMER BLAES

Department of Physics, University of California, Santa Barbara, CA 93106

AND

JULIAN H. KROLIK

Department of Physics and Astronomy, Johns Hopkins University, Baltimore, MD 21218

Received 1999 September 10; accepted 1999 November 30

ABSTRACT

We have constructed a grid of non-LTE disk models for a wide range of values of black hole mass and mass accretion rate, for several values of the viscosity parameter α , and for two extreme values of the black hole spin: the maximum-rotation Kerr black hole, and the Schwarzschild (nonrotating) black hole. Our procedure calculates self-consistently the vertical structure of all disk annuli together with the radiation field, without any approximations imposed on the optical thickness of the disk, and without any ad hoc approximations to the behavior of the radiation intensity. The total spectrum of a disk is computed by summing the spectra of the individual annuli, taking into account the general relativistic transfer function.

The grid covers nine values of the black hole mass between $M = 1/8 \times 10^9$ and $32 \times 10^9 M_\odot$ with a twofold increase of mass for each subsequent value; and eleven values of the mass accretion rate, each a power of 2 times $1 M_\odot \text{ yr}^{-1}$. The highest value of the accretion rate corresponds to the total luminosity $L/L_{\text{Edd}} \approx 0.3$. We show the vertical structure of individual annuli within the set of accretion disk models, along with their local emergent flux, and discuss the internal physical self-consistency of the models. We then present the full disk-integrated spectra and discuss a number of observationally interesting properties of the models, such as optical/ultraviolet colors, the behavior of the hydrogen Lyman limit region, polarization, and the number of ionizing photons. Our calculations are far from definitive in terms of the input physics, but generally we find that our models exhibit rather red optical/UV colors. Flux discontinuities in the region of the hydrogen Lyman limit are only present in cool, low-luminosity models, while hotter models exhibit blueshifted changes in spectral slope.

Subject headings: accretion, accretion disks — galaxies: active — galaxies: nuclei

1. INTRODUCTION

A black hole that steadily accretes gas from its surroundings at high rates, but below the Eddington limit, should form a geometrically thin accretion disk supported by the residual angular momentum of the gas. For black hole masses in the range 10^8 – $10^9 M_\odot$, thought to be typical of bright active galactic nuclei (AGNs) and quasars, the peak effective temperature is expected to be around 10^4 – 10^5 K. This estimate is roughly consistent with the observation that quasar spectra peak in the ultraviolet, bolstering the belief that quasars are indeed powered by accretion onto massive black holes.

Over the years, many authors have attempted to calculate detailed theoretical spectra of geometrically thin, optically thick accretion disks in order to compare with observation, with varying degrees of sophistication (e.g., Kolykhalov & Sunyaev 1984; Sun & Malkan 1989; Laor & Netzer 1989; Ross, Fabian, & Mineshige 1992; Shimura & Takahara 1993, 1995; Dörrer et al. 1996; Sincell & Krolik 1998). As reviewed recently by Krolik (1999a) and Koratkar & Blaes (1999), these and other models generally suffer from a number of problems when trying simultaneously to explain various features of the observations, e.g., optical/

ultraviolet continuum spectral shapes, the lack of observed features at the Lyman limit of hydrogen, polarization, the origin of extreme ultraviolet and X-ray emission, and correlated broadband variability. It may be that the resolution of these problems requires drastic revision of the accretion disk paradigm. Alternatively, it may simply be that the theoretical modeling to date is still too crude to do justice to the inherent complexities of the accretion flow. In particular, inclusion of non-LTE effects and detailed opacity sources, Comptonization, and interaction between the disk and X-ray-producing regions should all be taken into account.

We have embarked on a long-term program to construct detailed model spectra of accretion disks in the axisymmetric, time-steady, thin-disk approximation. At the peak temperatures, the most important opacity is provided by electron scattering, but bound-free and free-free continuum opacities due to hydrogen and helium can also be significant, so we include these opacities in this study. Since scattering can be the dominant opacity and the densities can be rather low, departures from local thermodynamic equilibrium (LTE) can be significant, so we include non-LTE effects as well. We include the effects of relativity on the disk

structure and on the transport of radiation from the disk to infinity. We construct a grid of models for a black hole spin of $a/M = 0$ (Schwarzschild black hole), and 0.998 (maximum rotation Kerr black hole), luminosities between $3 \times 10^{-4} L_{\text{Edd}}$ and $0.3 L_{\text{Edd}}$, and black hole masses between $M_{\text{g}} \equiv 10^{-9} M/M_{\odot} = 0.125$ to $M_{\text{g}} = 32$. To determine the surface mass density of the disk, we assume that the viscous stress scales as $t_{r\phi} = \alpha P_{\text{total}}$ (Shakura & Sunyaev 1973), where $t_{r\phi}$ and P_{total} are the vertically integrated viscous stress and total vertically integrated pressure, respectively.

In previous papers (Hubeny & Hubeny 1997 and 1998a, hereafter Papers I and II, respectively), we presented detailed spectra and the vertical structure of individual annuli. In this paper we integrate such spectra over radius for a grid of 99 mass/accretion rate combinations appropriate for quasars. We do not include annuli with low effective temperatures ($T_{\text{eff}} < 4000$ K) as these require molecular opacities for accurate computation. The spectra of hot annuli can be affected by Compton scattering, which we have not included in the calculation, but will in future work. It is likely that metal opacities will also modify the final spectrum (see Hubeny & Hubeny 1998b), so we consider this work as a benchmark for future metal line-blanketed models.

This paper is organized as follows. In § 2 we describe our model assumptions and computational methods. Then in § 3, which constitutes the bulk of the paper, we present our results. We start by showing the vertical structure of individual annuli within the set of accretion disk models, along with their local emergent flux. We then discuss the internal physical self-consistency of these models, before presenting the full disk-integrated spectra. We finish § 3 with a discussion of a number of observationally driven issues: optical/ultraviolet colors, spectra in the hydrogen Lyman limit region, polarization, and ionizing continua. Finally, in § 4 we summarize our conclusions, in particular pointing out the additional physics which will be included in future papers of this series.

2. MODEL ASSUMPTIONS AND COMPUTATIONS

To construct a model of an accretion disk, we assume the vertical disk structure can be well approximated by one-dimensional equations; that is, we assume the disk is locally plane parallel. We assume that, on average, the disk is static in the corotating frame (in reality disks are subject to many instabilities which invalidate this approximation) and that the only energy transport is due to radiation flux in the vertical direction, i.e., we ignore convection and conduction. By assuming time-steadiness and local radiation of dissipated heat, we can write down and solve the equations for the disk structure (Page & Thorne 1974); these equations are summarized in Paper II. For a given radius r , the (one-sided) flux (and thus the effective temperature, T_{eff}) is determined by

$$F(r) \equiv \sigma_{\text{B}} T_{\text{eff}}^4 = \frac{3GM\dot{M}}{8\pi r^3} R_{\text{R}}, \quad (1)$$

where σ_{B} is the Stefan-Boltzmann constant, \dot{M} the mass accretion rate, and R_{R} is a relativistic correction factor (Page & Thorne 1974, in the notation of Krolik 1999a). Following the usual practice for geometrically thin accretion disks, we assume that there is no torque at the innermost stable circular orbit in all our disk models. There are

reasons to question this assumption (Krolik 1999b; Gammie 1999); if it fails, the disk spectrum and polarization could be substantially changed (Agol & Krolik 2000).

We have calculated models for two values of the viscosity parameter: $\alpha = 0.01$ and $\alpha = 0.1$. The choice of $\alpha = 0.01$ is near the value expected from simulations of the magneto-rotational instability in accretion disks (e.g., Balbus & Hawley 1998), while $\alpha = 0.1$ represents a typical value of the viscosity parameter used in other studies. Smaller α or a stress which scales in proportion to the gas pressure would lead to a larger surface mass density, higher density, and, presumably, spectra closer to LTE.

If the disk rotates on cylinders and the angular frequency of each cylinder is the one appropriate to a circular orbit at the midplane, there is a vertical component to the effective gravity proportional to height z above the disk midplane. We ignore the self-gravity of the disk, an excellent approximation for the radii important to our problem.

We have assumed that the local dissipation is proportional to the local density, except for the top 1% of the disk, where we force the dissipation to decline (see Paper II). This distribution is chosen in order to yield a hydrostatic equilibrium solution in the bulk of the disk when radiation dominates (see Shakura & Sunyaev 1973), while retaining the possibility of thermal balance in the outermost layers even in the absence of Comptonization. In Paper II (in particular, see Figs. 11 and 12 there) we showed that neither the choice of the division point between the regions of vertically constant and declining viscosity nor the slope of the power law for the viscosity in the declining regime changes the predicted continuum emergent spectrum significantly. Disks with this structure can be convectively unstable, however. Convection can be expected to accelerate heat loss, leading to a disk structure that is rather thinner and denser (Bisnovatyi-Kogan & Blinnikov 1977), although perhaps not substantially so (Shakura, Sunyaev & Zilitinkevich 1978). Even annuli with entropy increasing upward, so that they are stable according to the usual Schwarzschild criterion, may still nevertheless be subject to convective instabilities mediated by thermal conduction along weak magnetic field lines (Balbus 1999). How this would manifest itself in the presence of turbulence driving the radial angular momentum transport is not clear, however. In any case, as stated above, we completely ignore convective heat transport in all our models here.

When either radiation or gas pressure dominates, the surface mass density may be readily calculated in the gray, one-zone, diffusion approximation. However, when the two are comparable to each other, the disk structure equations combine to form a single tenth-order polynomial equation in one of the variables (e.g., $\Sigma^{1/4}$). We solve this equation iteratively, using the two limiting regimes to bracket the root.

Once the effective temperature, surface mass density, and dissipation profile are determined, the vertical disk structure can be computed. To compute the vertical structure of a given annulus, we solve simultaneously the entire set of structural equations: hydrostatic equilibrium in the vertical direction; local energy balance; radiative transfer; and, since we are not generally assuming LTE, statistical equilibrium for all selected energy levels of all selected atoms and ions. The equations are solved for the whole extent of the disk between the midplane and the surface using proper boundary conditions. For details, the reader is referred to

Paper II. We stress that no ad hoc assumptions about the nature of the radiation field or the radiative transfer are made; for instance, we do not use the diffusion approximation or an escape probability treatment, or any assumption about the angular dependence of the specific intensity; the radiative transfer is solved exactly. To represent the radiation field, we use about 150 frequency points placed to define all continuum edges and resolve any frequency-dependent structure in the emergent intensity. The minimum frequency is set to 10^{12} Hz, while the highest frequency is chosen so that even at the midplane the intensity for frequencies higher than the maximum is negligible. In terms of the midplane temperature (Paper II and Hubeny 1990)

$$T_{\text{mid}} \approx T_{\text{eff}}(3\tau_{\text{mid}}/8)^{1/4} = T_{\text{eff}}[(3/8)(\Sigma/2)(\chi_{\text{R}})]^{1/4}; \quad (2)$$

Here this goal can be achieved by setting the maximum frequency to

$$v_{\text{max}} = 17kT_{\text{mid}}/h. \quad (3)$$

Here χ_{R} is the Rosseland mean opacity (per gram), which we take for simplicity to be 0.34, the value corresponding to an opacity dominated by electron scattering in a fully ionized H-He plasma of solar abundance.

We consider disks composed of hydrogen and helium only. We include metals in computing the molecular weight, but for this work, we ignore their effects on the opacity. Hydrogen is represented essentially exactly: the first eight principal quantum numbers are treated separately, while the upper levels are merged into a single non-LTE level accounting for level dissolution as described by Hubeny, Hummer, & Lanz (1994). We do, however, assume complete l -mixing; given the high electron density in these environments, this should be a good approximation. Neutral helium is represented by a 14-level model atom, which incorporates all singlet and triplet levels up to $n = 8$. The five lowest levels are included individually; singlet and triplet levels are grouped separately from $n = 3$ to $n = 5$, and we have formed three superlevels for $n = 6, 7$, and 8 . The first 14 levels of He^+ are explicitly treated. We assume a solar helium abundance, $N(\text{He})/N(\text{H}) = 0.1$.

The opacity sources we include are all bound-free transitions (continua) from all explicit levels of H, He I, and He II; free-free transitions for all three ions, and electron scattering. For the coolest models ($T_{\text{eff}} < 9000$ K), we also consider the H^- bound-free and free-free opacity, assuming LTE for the H^- number density. In this paper, we assume coherent (Thomson) scattering. As was discussed in Paper II, effects of noncoherent (Compton) scattering are negligible for models with T_{eff} around or below 10^5 K. Therefore, most models of the present grid (see § 3) are not influenced by the effects of Comptonization, although the hottest ones may be. We have recently implemented Comptonization in our modeling code and checked that this is indeed the case; however, we choose to neglect Comptonization in this paper in order to provide a benchmark grid of models computed using classical approximations of H-He composition and without Comptonization. The effects of Compton scattering will be included in a future paper, where we will also discuss in detail its influence on the emergent spectra. It can be expected to become especially important when the dissipation per unit mass is enhanced near the disk's surface.

The structure equations are highly nonlinear, but are very similar to corresponding equations for model stellar

atmospheres. We use here the computer program TLUS-DISK, which is a derivative of the stellar atmosphere program TLUSTY (Hubeny 1988). The program is based on the hybrid complete-linearization/accelerated lambda iteration (CL/ALI) method (Hubeny & Lanz 1995). The method resembles traditional complete linearization, but the radiation intensity in most (but not necessarily all) frequencies is not linearized; instead it is treated via the ALI scheme (for a review of the ALI method, see e.g., Hubeny 1992). Moreover, we use Ng acceleration and the Kantorovich scheme (Hubeny & Lanz 1992) to speed the solution. We start with a gray atmosphere solution (Hubeny 1990), first solving for the disk structure assuming that the statistical equilibrium is described by LTE. Using this as a starting point, we drop the LTE assumption and compute the disk structure using the full statistical equilibrium equations, as described in Paper II, but assuming that the line transitions are in detailed radiative balance. In other words, the statistical equilibrium equations explicitly contain the collisional rates in all transitions, and radiative rates only in the continuum transitions. We have considered 70 discretized depth points. The top point is set to $m_1 = 10^{-3}$ g cm^{-2} , where m is the column mass, i.e., the mass in a column above a given height. The last depth point is the column mass corresponding to the midplane, and is given by $\Sigma/2$. The depth points are equally spaced in logarithm between these two values. The models were computed on a DEC Alpha with 500 MHz clock speed; with the above values for the number of frequency and depth points, the LTE models for individual rings required typically 5–10 iterations with approximately 2.5 s per iteration, while the non-LTE models required typically 5–10 (for hotter annuli) or 10–30 iterations (for cooler annuli), with about 6 s per iteration.

We do not compute here models treating radiative rates in line transitions explicitly. We have considered such models in Paper II and found that including lines explicitly does not change the vertical structure or emergent continuum radiation significantly. These models are also much more time consuming. However, the most important physical point is that we have found in test calculations that line profiles are influenced significantly by the effects of Compton scattering. Since we are neglecting the Comptonization here to provide a benchmark grid of classical H-He models without Comptonization, we feel that including lines at this stage would not be much more than a numerical exercise. We therefore defer treatment of more realistic models including lines and Comptonization to a future paper.

In the course of calculating atmosphere models, we sometimes ran into difficulties with convergence. For very low and very high temperatures, we could not get convergence, a problem which may be ameliorated in the future by including more sources of opacity (such as metals at high temperatures and molecules at low temperatures). At certain radii and certain depths within the disk, we found ionization fronts in helium around $T_{\text{eff}} \sim 35,000$ K which are very narrow in extent and very sensitive to the temperature within the disk, causing limit cycle behavior where the helium alternates between being mostly doubly ionized or recombined to a singly ionized stage during successive steps, preventing solution of the atmosphere structure. We solved this problem by computing the disk structure for radii just smaller or larger than the radii where the front

exists and then using these solutions as starting solutions for the radii at which the fronts exist. In practice, the range of radii where this problem exists is narrow so that the uncertainty in the structure does not affect the overall disk spectrum. We also found similar He I/He II ionization fronts at lower temperatures, $T_{\text{eff}} \sim 15,000$ K, and for hydrogen around and below 9000 K.

To find the total disk spectrum, we divided the disk into 25–35 radial rings, spaced (roughly) logarithmically. At each ring, after computing the vertical structure, we perform a detailed radiation transfer solution for the Stokes vector as a function of frequency and angle. The spectrum is found by integrating the total emergent intensity over the disk surface using our relativistic transfer function code (Agol 1997). The transfer function computes the trajectories of photons from infinity to the disk plane, finding the emitted radius, redshift, and intensity at each image position at infinity for a given observation angle (Cunningham 1975). In this paper, we neglect the effects of radiation which returns to the accretion disk.

3. RESULTS

The parameter space of our grid of models is displayed in Figure 1. The defining parameters are M_9 , the black hole mass expressed in $10^9 M_\odot$, and \dot{M} , the accretion rate in units of $M_\odot \text{ yr}^{-1}$. The grid covers nine values of the black hole mass between $M_9 = 1/8$ and 32; each subsequent mass is twice the previous mass. An analogous approach is used for the mass accretion rate, i.e., eleven values for each black hole mass which are powers of 2 times $1 M_\odot \text{ yr}^{-1}$. The highest value of the accretion rate in each case is chosen to make $L/L_{\text{Edd}} = 0.286$; i.e., $\dot{M}(M_\odot \text{ yr}^{-1}) = 2M_9$. In the following text, we refer to this highest value as $L/L_{\text{Edd}} = 0.3$. The ten subsequent values have half the accretion rate (and luminosity) of the previous model. Our grid spans a range similar to models which have been previously used to fit quasar spectra (Sun & Malkan 1989; Laor 1990).

Our basic grid assumes $a/M = 0.998$. However, we have also constructed a parallel grid for a Schwarzschild black hole with the same black hole masses and values of L/L_{Edd} . The mass accretion rates for $a/M = 0$ are a factor of 5.613 higher than the corresponding values for $a/M = 0.998$ because the radiative efficiency of a Kerr disk is that much greater (e.g., Shapiro & Teukolsky 1983).

For all disk models, we compute detailed vertical structure at the following radii (expressed as r/r_g , where $r_g = GM/c^2$ is the gravitational radius): $r/r_g = 1.5, 1.7, 2, 2.5, 3, 3.5, 4, 5, 6, 7, 8, 9, 10, 12, 14, 16, 18, 20, 25, 30, 40, 50, 60, 70, 80, 90, 100, 120, 140, 160, 180, 200, 250, 300, 400, \text{ and } 500$; that is, while the corresponding effective temperature $T_{\text{eff}} > 4000$ K. For the Schwarzschild grid, we use the above values of r/r_g , multiplied by 5. The actual number of computed annuli thus depends on the basic parameters of the disk.

3.1. Properties of Models

In this section, we discuss the behavior of individual annuli, while in the rest of the paper we will present the emergent radiation integrated over the whole disk. We have chosen a model with $M_9 = 1$, $\dot{M} = 1$ (i.e., $L/L_{\text{Edd}} = 0.15$) as a representative model for displaying various quantities. The behavior of other individual disk models is similar. Figure 2 displays the local electron temperature as a func-

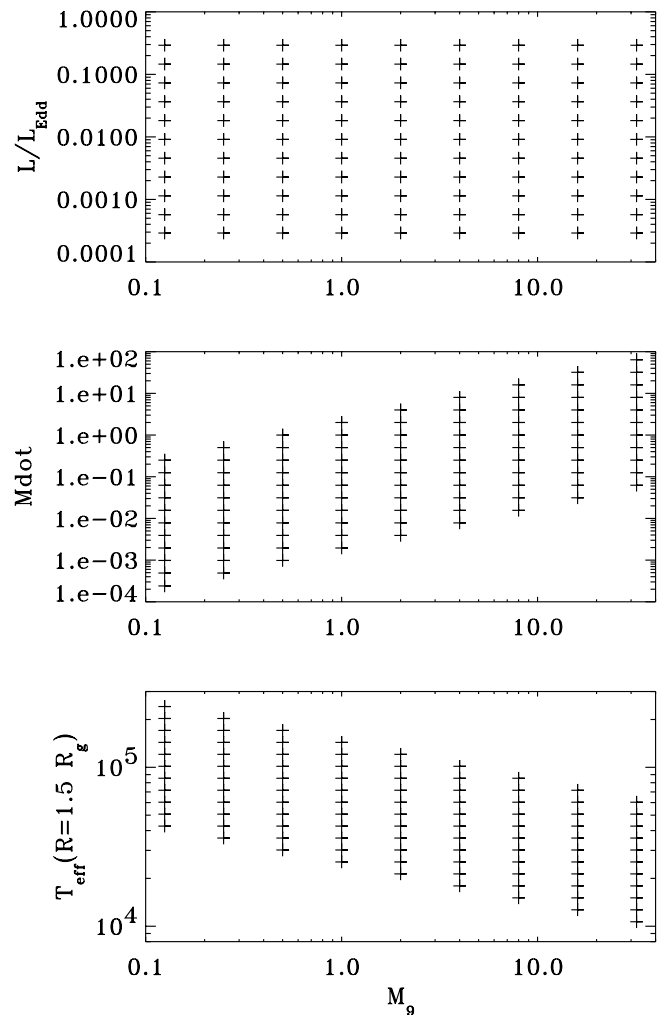


FIG. 1.—Parameters of our grid of disk models for the Kerr hole case. *Upper panel:* L/L_{Edd} vs. black hole mass, expressed in $10^9 M_\odot$. *Middle panel:* the mass accretion rate, \dot{M} , expressed in $M_\odot \text{ yr}^{-1}$. *Lower panel:* the maximum effective temperature (which is found at $r \approx 1.5r_g$).

tion of position for all individual annuli. The position is expressed as column mass, m , above the given depth. As mentioned in § 2, the uppermost point was chosen to be $m = 10^{-3} \text{ g cm}^{-2}$, while the highest value corresponds to the midplane of the disk. The temperature is a nearly monotonic function of depth, although there is a slight temperature rise at the surface for some models. The detailed behavior of temperature for several representative annuli was discussed extensively in Paper II. The behavior of temperature for all annuli is easily understood. In the LTE approximation, the midplane temperature is given by equation (2), i.e., it is proportional to $T_{\text{eff}}(r)[m_0(r)]^{1/4}$, where $m_0 \equiv \Sigma/2$ is the total column density at the midplane. Neglecting for simplicity the relativistic corrections, $T_{\text{eff}} \propto r^{-3/4}$ (see eq. [1]), while the column density $m_0 \propto r^{3/2}$ for radiation pressure-dominated annuli (see eq. [18] of Paper II), which is the case for the models considered in Figure 2. Therefore, the LTE approximation predicts that the midplane temperature, $T_{\text{mid}} \propto r^{-3/8}$. In contrast, the surface temperature is proportional to T_{eff} ; therefore, $T_{\text{surf}} \propto r^{-3/4}$. Figure 2 shows that these scalings do in fact hold approximately. The ratio of the lowest and highest radii is roughly

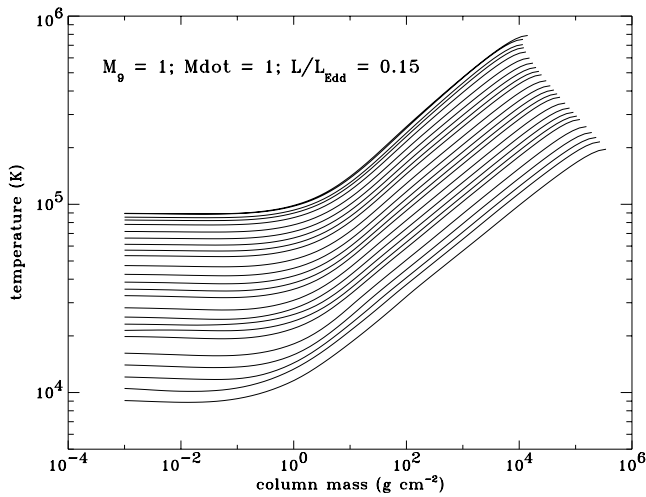


FIG. 2.—Temperature as a function of depth for the individual annuli. The curves correspond to radii r/r_g (from top to bottom) 1.5, 2, 2.5, 3, 3.5, 4, 5, 6, 7, 8, 9, 10, 12, 14, 16, 18, 20, 25, 30, 40, 50, 60, 70, 80, and 90.

45, so if the LTE approximation held, the local temperature would vary by a factor of 17 at the surface, and by a factor of 4.2 at the midplane. The model values are 14 and 4.6, respectively.

Figure 3 displays the run of mass density for the individual annuli. The central density is lowest for the inner annuli, and increases with increasing distance from the black hole, while the density close to the surface exhibits a more or less reverse behavior. Note that the disk becomes optically thin below a column mass of $m \simeq \chi_R^{-1} \simeq 2.9 \text{ g cm}^{-2}$, where the density is substantially lower (in some cases by orders of magnitude) than the midplane density. This should be borne in mind when comparing our results to those of previous workers who assumed constant density slabs (e.g., Laor & Netzer 1989). An explanation of the behavior of the density is given in the Appendix.

A more interesting behavior is exhibited by the H I and He II ground state number densities, displayed in Figures 4 and 5. For hot, inner annuli, hydrogen remains ionized

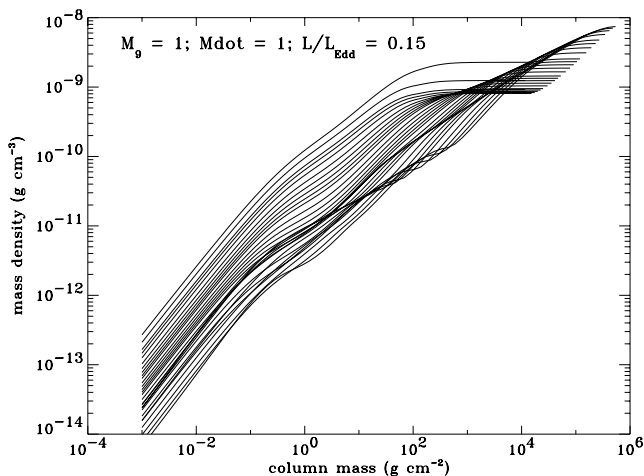


FIG. 3.—Mass density as a function of depth for the individual annuli. The radii are the same as in Fig. 2. At the midplane, the highest density corresponds to the largest r/r_g (equal to 90), while the lowest density corresponds to $r/r_g = 2.5$. The two uppermost curves for $m < 10^3$ correspond to $r/r_g = 1.5$ and 2, respectively.

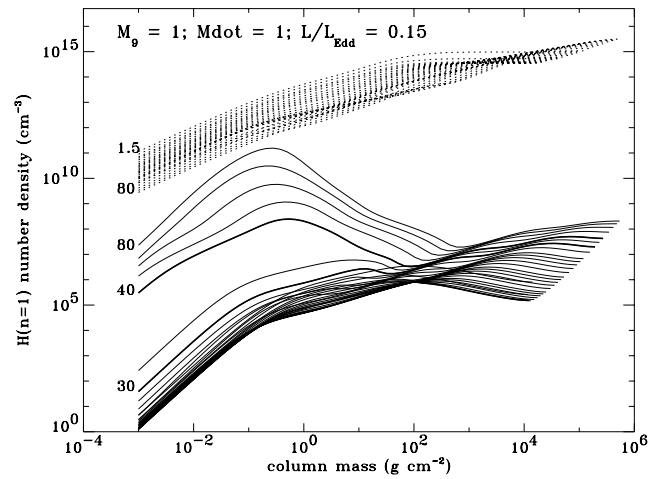


FIG. 4.—Number density of the ground state of H I as a function of depth (solid lines), and the proton number density (dotted lines). The radii are the same as in Fig. 2. Selected models are labeled by the radial coordinate, r/r_g , and the models for $r/r_g = 30$ and 40, which delimit the regions between the full and partial ionization of hydrogen, are drawn by bold lines.

throughout the entire vertical extent of the disk, while starting with the annulus at $r = 40r_g$ (with $T_{\text{eff}} \approx 15,000 \text{ K}$), there is an appreciable portion of neutral hydrogen in the outer layers ($m < 10^2 \text{ g cm}^{-2}$). Consequently, the Lyman edge opacity for these latter models becomes rather large (see below). Similarly, helium exhibits a transition, between $r = 12r_g$ (with $T_{\text{eff}} \approx 36,000 \text{ K}$) and $r = 14r_g$ (with $T_{\text{eff}} \approx 32,500 \text{ K}$) from being predominantly doubly ionized, to a situation where the single ionized helium is a dominant stage of ionization at some outer part of the disk. For the annuli with $r < 40r_g$ (with $T_{\text{eff}} > 15,000 \text{ K}$), helium remains singly ionized throughout the entire upper part of the disk, while for more distant, cooler annuli, neutral helium becomes more and more dominant in the outer layers. Figure 6 displays the emergent flux for all annuli. The upper panel shows the non-LTE models, while the lower panel shows the LTE models. The behavior of the emergent flux is analogous to that discussed at length in Papers I and II.

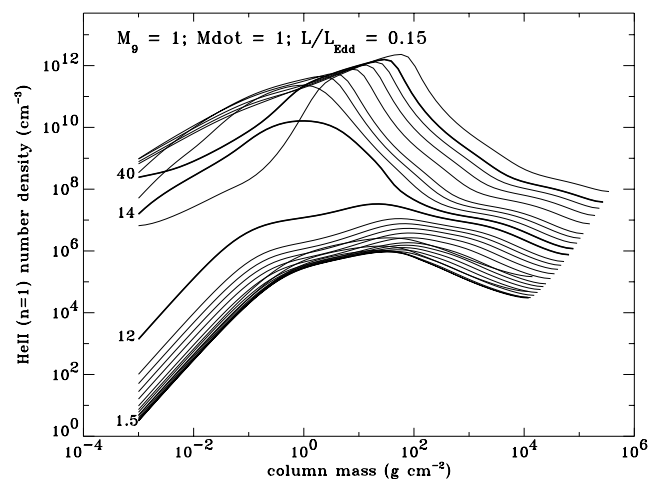


FIG. 5.—Number density of the ground state of He II as a function of depth. The radii are the same as in Fig. 2. Selected models are labeled by the radial coordinate, r/r_g , and the models for $r/r_g = 12$, 14, and 40, are drawn by bold lines.

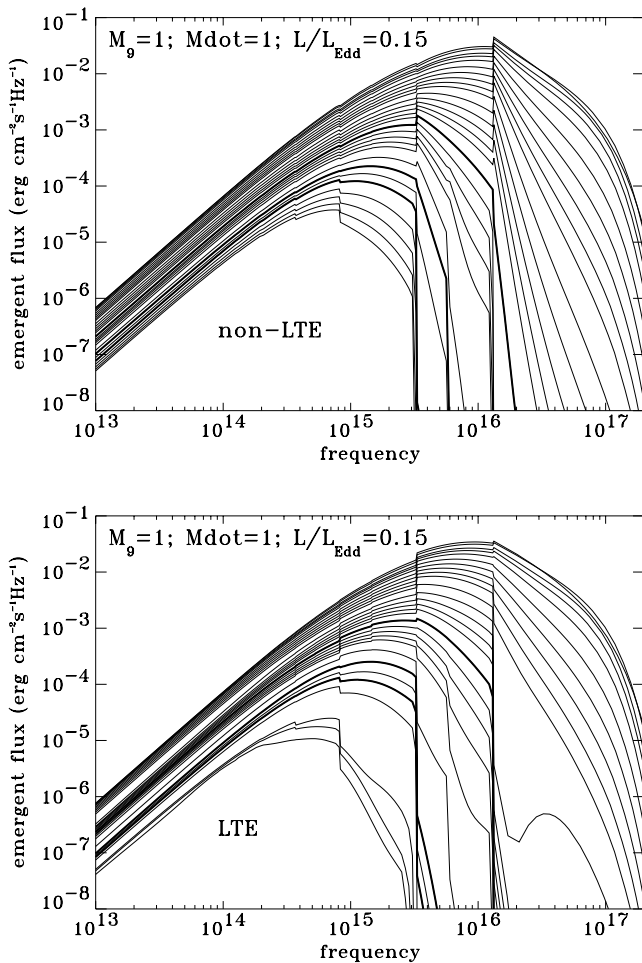


FIG. 6.—Predicted local emergent flux (in ergs cm s⁻¹ Hz⁻¹) for the individual annuli for non-LTE models (*upper panel*), and LTE models (*lower panel*). The models for $r/r_g = 12, 30,$ and $40,$ are drawn by bold lines.

Non-LTE models exhibit the He II Lyman edge in emission for $r < 12r_g$ (with $T_{\text{eff}} > 36,000$ K), while for more distant annuli the flux in the He II Lyman continuum drops to almost zero. This is a consequence of the transition from the dominance of double-ionized helium to singly-ionized helium, as displayed in Figure 5. Analogously, the neutral-hydrogen annuli for $r > 40r_g$, with $T_{\text{eff}} > 15,000$ K (see Fig. 4), show a significant hydrogen Lyman edge in absorption.

A comparison between LTE and non-LTE results reveals several interesting effects: in LTE, the He II Lyman edge appears to be in weaker emission or even in absorption for hot, doubly-ionized, annuli. Most importantly, non-LTE effects reduce the hydrogen Lyman edge (cf. Sun & Malkan 1989; Shields & Coleman 1994; Störzer, Hauschildt, & Allared 1994; Papers I and II): the edge predicted in non-LTE models is typically in weaker emission for emission edges and in weaker absorption for absorption edges. We discuss the behavior of the hydrogen Lyman edge in the full disk-integrated spectra in more detail in § 3.5 below.

Finally, Figure 7 shows a comparison of predicted local non-LTE flux and the blackbody flux corresponding to the same effective temperature. As already discussed in Paper I, the non-LTE models exhibit a much wider spectral energy distribution than blackbodies. Consequently, an often-used mapping of a given spectral region to a certain radial posi-

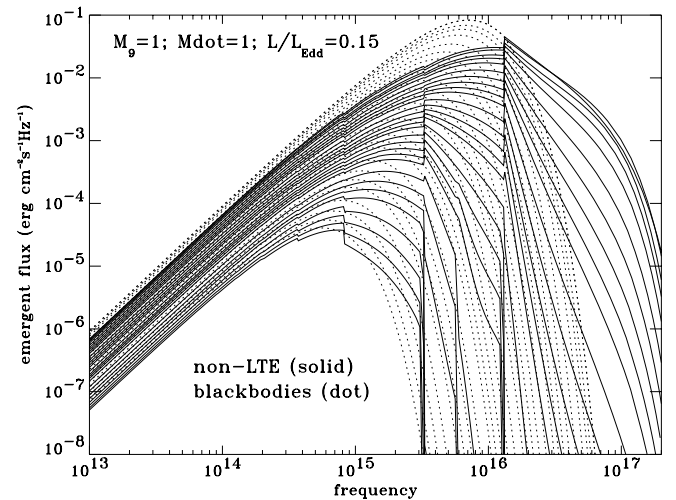


FIG. 7.—Predicted local emergent flux (in ergs cm s⁻¹ Hz⁻¹) for the individual annuli for non-LTE models (*solid lines*), together with a blackbody flux corresponding to the same effective temperature as the given annulus (*dotted lines*).

tion in the disk, which may be used for a blackbody flux because of its sharp variation with frequency, is much less satisfactory for more realistic non-LTE vertical structure models. Another crucial feature of the present models is that compared to blackbodies the energy is redistributed. At low temperatures, absorptive opacity is relatively important, so that flux is shifted from frequencies where the opacity is high to frequencies where it is low; i.e., away from ionization edges. Another way of viewing this effect is to note that in bands where the opacity is low, escaping photons are created deeper inside the disk where the temperature is higher. At high temperatures, the opacity becomes scattering-dominated. In these rings, there is a trade-off between the effect just mentioned (lower opacity bands allow one to see photons created at higher temperature) and scattering blanketing (which retards the escape of photons created deep inside). The latter effect is the one that creates a “modified blackbody” spectrum when there is no temperature gradient. For much of the parameter range of interest, the net effect is to shift flux toward higher frequencies.

3.2. Consistency of Models

Having computed the detailed vertical structure of the annuli, we have to address the question of self-consistency of the model assumptions.

First, we check that the computed disks are indeed geometrically thin, i.e., the disk height, H , is much smaller than the radial coordinate r . In Figure 8 we show the ratio of the disk height to the radial coordinate, H/r , as a function of the radial coordinate (in units of gravitational radius), for a disk with $M_g = 1$, and for various values of \dot{M} (or luminosity). The behavior of disks for other values of the black hole mass is almost identical. (This is expected for radiation pressure-supported, electron scattering-dominated disks, because then H/r can be written as L/L_{Edd} times a function of r/r_g ; see eq. [53] of Paper II.) Only for the most luminous disk does the ratio H/r approach 10% at $r/r_g = 2.5$. The height of other annuli is lower, and the maximum height for less luminous disks is progressively lower. These results are in good agreement with the older models of Laor & Netzer

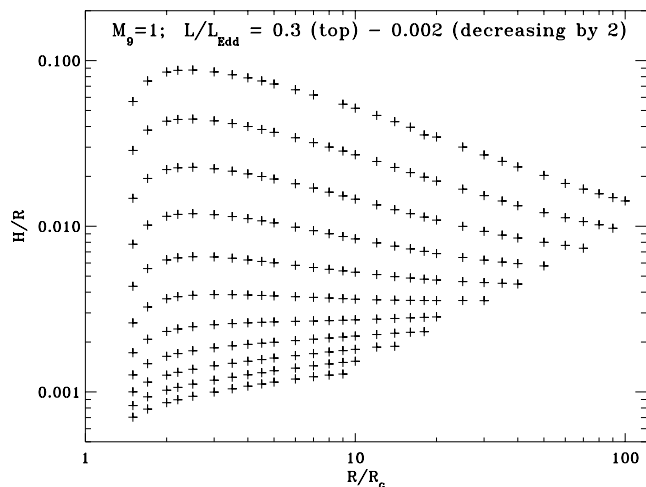


FIG. 8.—Ratio of the disk height to the radial coordinate, H/r , as a function of the radial coordinate (in units of gravitational radius), for a disk with $M_g = 1$, and for various values of \dot{M} (or luminosity). The crosses represent the actual computed models of the individual annuli.

(1989; cf. their Fig. 1 and the surrounding discussion). We therefore conclude that our disks do indeed satisfy the thin disk approximation.

Another important concern is the presence of vertical density inversions within the disk. Since we neglect convection, sharp temperature gradients and density inversions are found at ionization transitions occurring in regions where gas pressure contributes significantly to support against gravity. In Figure 9 we display the structure of several annuli that illustrate this behavior. The hottest annulus shown in that figure ($r/r_g = 50$) has $T_{\text{eff}} = 9400$ K; it is the outermost ring with no density inversion. Cooler, more distant annuli show a progressively stronger inversion. The inversion is created by the abrupt fall in electron density when H recombines; in order to maintain the pressure gradient required for hydrostatic balance, the mass density must increase to compensate. A sharp rise of local temperature, displayed in the upper panel of Figure 9, is caused by a rapid increase of opacity when going inward due to an ionization front. The temperature is essentially a function of the Rosseland mean opacity, $T \propto \tau_{\text{Ross}}^{1/4}$, but since τ_{R} is a sharp function of the column mass m , the function $T(m)$ also exhibits a sharp increase with m .

These models should be taken with caution. In the absence of detailed hydrodynamical calculations which would allow for convective instability and determine the vertical structure properly, we do not know what is the correct emergent radiation. We can nevertheless obtain a rough indication of model uncertainties by comparing the predicted flux from the non-LTE models that neglect convection, and a blackbody flux corresponding to the same effective temperature.

We present in Figure 10 emergent flux for three selected annuli shown in Figure 9, for $r/r_g = 50, 90,$ and 160 , with corresponding effective temperature equal to $9400, 6200,$ and 4100 K, respectively. The predicted flux for non-LTE models is shown together with the corresponding blackbody flux. We see that the models at the hotter end of the density inversion sequence exhibit an appreciable Balmer edge, while the cooler models are reasonably well approximated by blackbodies. We thus feel that approximating

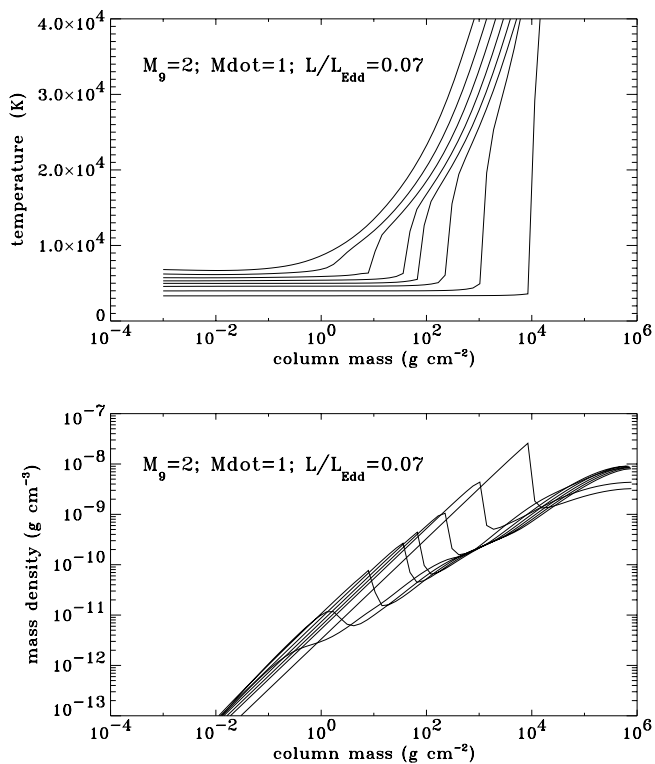


FIG. 9.—Upper panel: temperature as a function of position for a disk with $M_g = 2$ and $\dot{M} = 1 M_{\odot} \text{ yr}^{-1}$, for “cool” annuli (for radii $50, 60, 70, 80, 90, 100, 120,$ and $160 r_g$). The corresponding T_{eff} 's are $9400, 8300, 7400, 6700, 6200, 5700, 5000,$ and 4100 K. Lower panel: mass density for the same annuli.

even cooler models, which we do not compute here, by blackbodies is probably not worse than other approximations that underlie the entire calculation.

3.3. Disk-integrated Spectra

In this section, we present disk-integrated spectra for selected disk models. The full grid of models is not present-

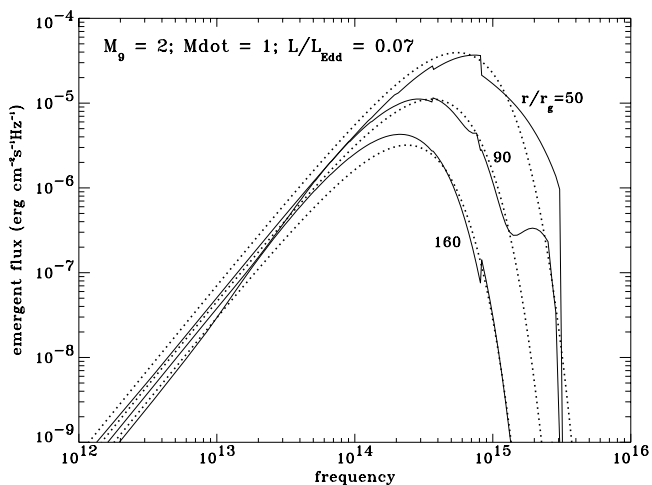


FIG. 10.—Predicted local emergent flux (in $\text{ergs cm}^{-2} \text{ s}^{-1} \text{ Hz}^{-1}$) for three selected annuli shown in Fig. 9. Solid lines: non-LTE models; dotted lines: blackbody flux corresponding to the same effective temperature as the given annulus. The curves are labeled by the value of $r/r_g = 50, 90,$ and 160 ; the corresponding $T_{\text{eff}} = 9400, 6200,$ and 4100 K, respectively.

ed here, but is available to interested researchers upon request.

Note that in all the spectral energy distributions shown in this paper, the quantity L_ν is the specific luminosity that an observer along a particular viewing angle would infer the source to have if it were isotropic, i.e., if F_ν is the measured specific flux and d is the distance to the source, then $L_\nu \equiv 4\pi d^2 F_\nu$. In the subsequent plots, we display, as is customary, the quantity νL_ν , which represents a luminosity per unit logarithmic interval of frequency (photon energy).

As discussed above, we consider the spectra of the outer annuli which were not computed (for $T_{\text{eff}} < 4000$ K) to be given by the black-body energy distribution corresponding to the effective temperature of the annulus. An important parameter is the outer cutoff of the disk. In order to avoid problems with an improper choice of the outer cutoff, we have chosen the cutoff radius r_{out} in such a way that $T_{\text{eff}}(r_{\text{out}})$ is equal to a specific limiting temperature, T_{lim} . We have chosen $T_{\text{lim}} = 1000$ K, which guaranties that the total emergent flux at $\nu = 10^{14}$, which is the lowest frequency considered in our integrated disk spectra, is not significantly influenced by cooler annuli with $T_{\text{eff}} < T_{\text{lim}}$ to within a few percent.

Figure 11 shows the effect of the outer cutoff, as well as of the degree of approximation in the treatment of cool annuli, for the disk model displayed in Figure 9 ($M_g = 2$; $\dot{M} = 1 M_\odot \text{ yr}^{-1}$, i.e., $L/L_{\text{Edd}} = 0.07$). Three cutoff radii are shown: $r_{\text{out}}/r_g = 60$, which is the radius where the density inversion sets in; $r_{\text{out}}/r_g = 160$ (the radius where T_{eff} reaches our minimum value of 4000 K), and finally the default value which corresponds to $T_{\text{lim}} = 1000$ K, which in this case happens at $r_{\text{out}}/r_g \approx 1060$. Neglecting all annuli cooler than 9000 K (*dotted line*) does not influence the flux blueward of the Balmer limit, but the optical and IR flux are seriously underpredicted. Neglecting all noncomputed annuli cooler than 4000 K (*dashed lines*) produces the correct flux in the region of the Balmer edge, and very nearly the correct flux in the optical range ($\nu > 4 \times 10^{14}$ Hz). The effect of uncer-

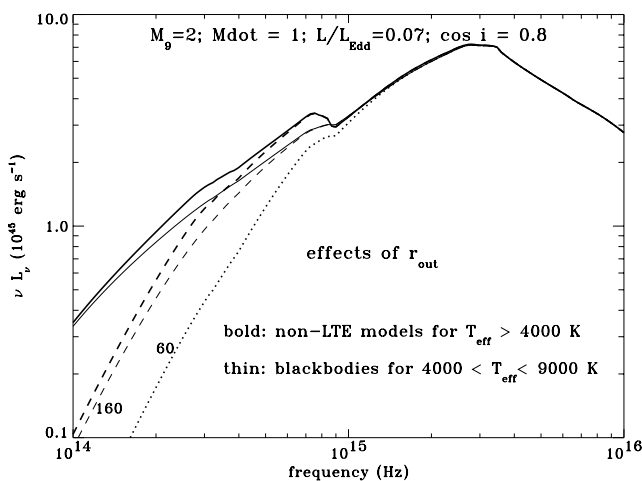


FIG. 11.—Integrated spectral energy distribution νL_ν for a disk with $M_g = 2$ and $\dot{M} = 1 M_\odot \text{ yr}^{-1}$ ($L/L_{\text{Edd}} = 0.07$), with inclination $\cos i = 0.8$, and with various choices of r_{out} . *Solid lines*: the automatic choice of r_{out} , corresponding to $T_{\text{lim}} = 1000$ K (in this case, $r_{\text{out}}/r_g \approx 1060$). *Dashed lines*: $r_{\text{out}}/r_g = 160$. *Dotted line*: $r_{\text{out}}/r_g = 60$; the curves are labeled by the value of r_{out}/r_g . Bold lines correspond to spectra computed for non-LTE models down to $T_{\text{eff}} = 4000$ K; thin lines show the spectra computed by replacing the local spectra of annuli with $T_{\text{eff}} < 9000$ K by blackbodies.

tainties in the models with density inversion ($T_{\text{eff}} < 9000$ K) is estimated by comparing bold lines, which show spectra computed for non-LTE models down to $T_{\text{eff}} = 4000$ K, with the corresponding thin lines, showing the predicted integrated spectra when all annuli with $T_{\text{eff}} \leq 9000$ K are assumed to emit locally as blackbodies. The maximum difference in the integrated spectra is found redward of the Balmer edge; the non-LTE models of cool annuli produce an integrated flux that is about 16% higher than that corresponding to replacing the $T_{\text{eff}} < 9000$ K annuli by blackbodies. Therefore, the effect is not very large, which gives us confidence that our overall integrated spectra are not significantly influenced by the uncertainties associated with the density inversions present in the cool annuli. However, the predicted feature at the Balmer edge should be viewed with caution.

We first present integrated spectra for a disk of given mass and luminosity, $M_g = 1$, $L/L_{\text{Edd}} = 0.15$ (i.e., $\dot{M} = 1 M_\odot \text{ yr}^{-1}$), and for various values of the inclination angle i , ranging from $\cos i = 0.99$ (i.e., the disk seen almost face-on) to $\cos i = 0.01$ (the disk seen almost edge-on) (see Figure 12). We can clearly see the impact of relativistic boosting and aberration: the flux at the highest frequencies (radiated where the disk is most relativistic) is boosted strongly for viewing angles near the disk plane. Also for such viewing angles, gravitational light bending counteracts the Newtonian “ $\cos \theta$ ” projection effect.

In the following, we present the integrated spectra for one value of inclination. We chose $\cos i = 0.8$ (i.e., $i \approx 37^\circ$), which is a value relatively close to face-on, and which thus may serve as a typical value for type 1 AGN and QSOs based on unification arguments (e.g., Krolik 1999a). Figure 13 shows the integrated spectra for one particular value of the black hole mass, $M_g = 1$, and for various luminosities (mass accretion rates). Solid lines display non-LTE models, while the dotted lines display LTE model predictions. The spectral energy distribution is hardest for the largest luminosity. The non-LTE effects are most important in the He II Lyman continuum ($\nu > 1.36 \times 10^{16}$ Hz), and also for predicting the detailed shape of the hydrogen Lyman edge for intermediate and low luminosities.

In Figure 14 we display the sequence of predicted spectra for models with a fixed mass accretion rate (i.e., total

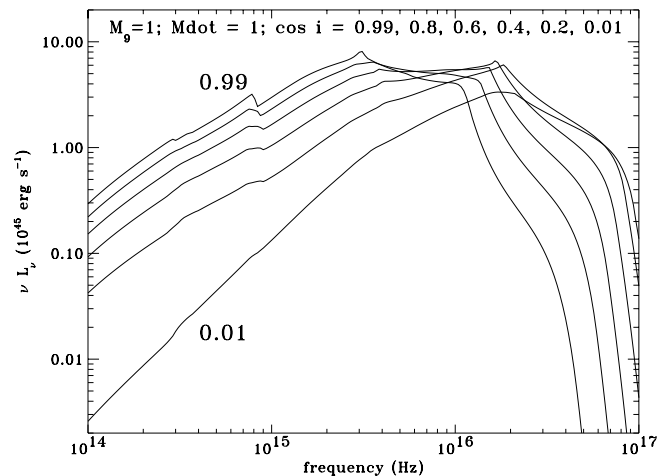


FIG. 12.—Integrated spectral energy distribution νL_ν (in ergs s^{-1}) for a disk with $M_g = 1$, $\dot{M} = 1 M_\odot \text{ yr}^{-1}$, and for various inclinations.

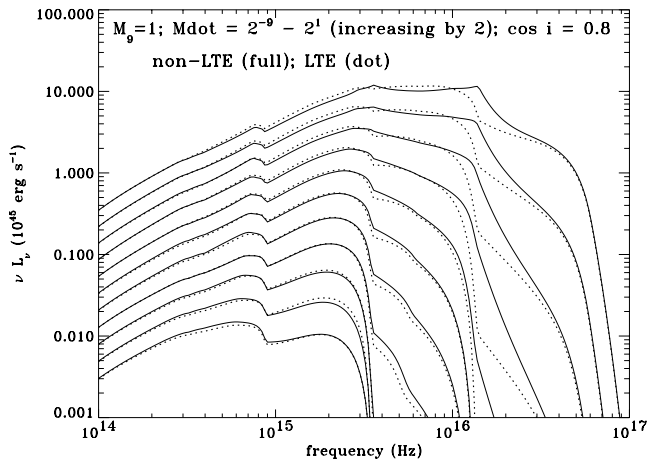


FIG. 13.—Integrated spectral energy distribution νL_ν (in ergs s^{-1}) for a disk with $M_0 = 1$, $\cos i = 0.8$, and for various values of the mass accretion rate (luminosity), ranging from $L/L_{\text{Edd}} = 0.3$ (i.e., $\dot{M} = 2 M_\odot \text{ yr}^{-1}$) to $L/L_{\text{Edd}} = 3 \times 10^{-4}$ (i.e., $\dot{M} = 2^{-9} M_\odot \text{ yr}^{-1}$). *Solid lines*: non-LTE models; *dotted lines*: LTE models.

luminosity) and varying black hole mass. The energy distribution is progressively shifted toward more energetic photons for lower masses, because disks around less massive holes have smaller radiating surface areas. The non-LTE effects are important for all disks; for hotter ones the largest departures from LTE are seen in the He II Lyman continuum, and in cooler ones in the hydrogen Lyman continuum.

Figure 15 shows the spectral energy distribution for a sequence of disk models which have the same $T_{\text{eff}}(r/r_g)$ distribution. Since

$$T_{\text{eff}}^4 \propto M \dot{M} r^{-3} R_{\text{R}}(r/r_g) \propto M^{-2} \dot{M} (r/r_g)^{-3} R_{\text{R}}(r/r_g), \quad (4)$$

the same T_{eff} distribution is obtained for models with fixed \dot{M}/M^2 . If disks radiated as blackbodies, all the spectra of the sequence would be exactly the same, only vertically shifted in the absolute value of the emergent flux. Indeed, the spectra are similar in the long-wavelength (optical and IR) portion of the spectrum, but they differ appreciably in the UV and EUV spectral region. In particular, the Lyman

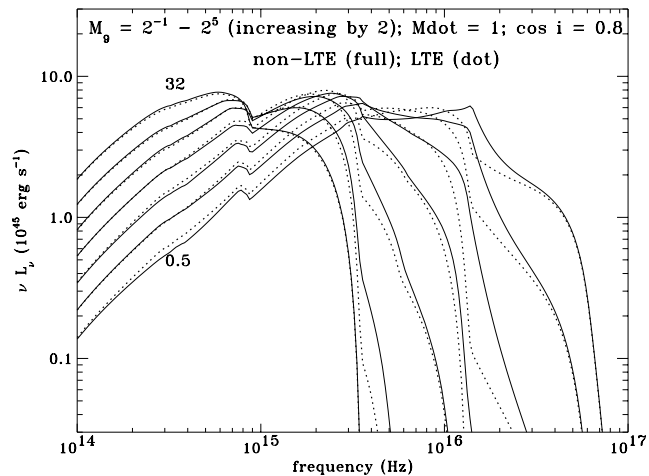


FIG. 14.—Integrated spectral energy distribution νL_ν (in ergs s^{-1}) for a disk with $\dot{M} = 1 M_\odot \text{ yr}^{-1}$, $\cos i = 0.8$, and for various values of the black hole mass, M_0 , ranging from $M_0 = 32$ – 0.5 .

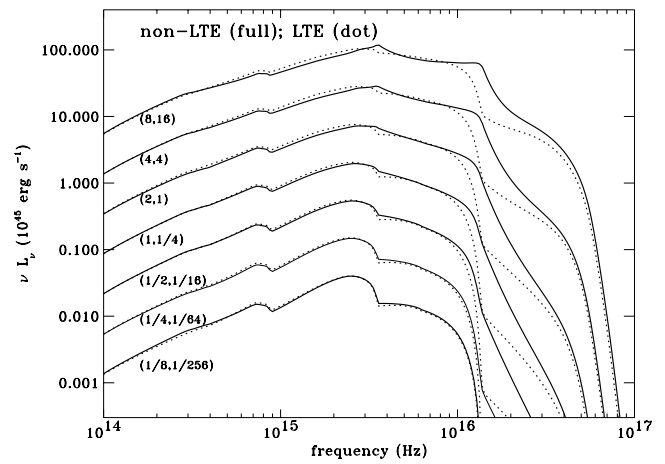


FIG. 15.—Integrated spectral energy distribution νL_ν (in ergs s^{-1}) for the pairs of (M_0, \dot{M}) which have the same effective temperature distribution, $T_{\text{eff}}(r/r_g)$, and which should therefore have a rather similar spectrum shape. The curves are labeled by the values of (M_0, \dot{M}) . *Solid lines*: non-LTE models; *dotted lines*: LTE models.

edges of hydrogen and He II change their appearance significantly. Note that the non-LTE and LTE models for lower black hole masses in this figure are very nearly the same. This is expected, as the average density $\rho \propto M/\dot{M}^2$ times some function of r/r_g for radiation pressure-dominated annuli. Hence for fixed \dot{M}/M^2 , ρ scales as M^{-3} , implying that the lower black hole mass models in Figure 15 have higher average densities and should therefore be closer to LTE.

Finally, in Figure 16 we present a sequence of models with the same L/L_{Edd} . Since $L/L_{\text{Edd}} \propto \dot{M}/M$, we chose a sequence where M_0 and \dot{M} (in $M_\odot \text{ yr}^{-1}$) have the same value; the corresponding $L/L_{\text{Edd}} = 0.15$. Again, the shape of the spectrum is quite similar in the optical and IR regions, while there is a progressively larger portion of EUV radiation for lower black hole masses. The non-LTE effects are

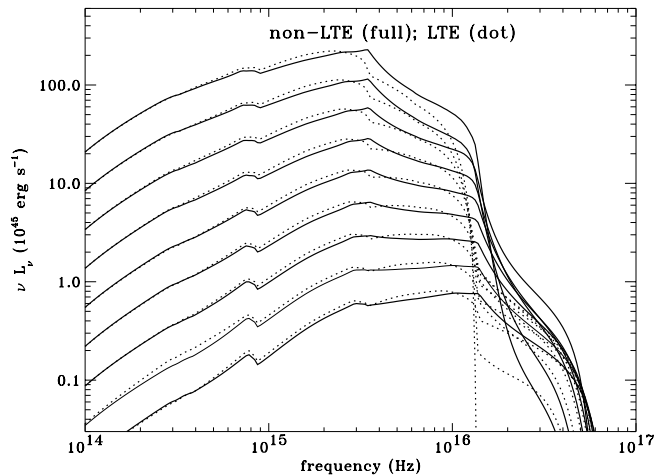


FIG. 16.—Integrated spectral energy distribution νL_ν (in ergs s^{-1}) for the pairs of (M_0, \dot{M}) which have the same $L/L_{\text{Edd}} = 0.15$. The numerical values of M_0 and \dot{M} expressed in $M_\odot \text{ yr}^{-1}$, are the same; the upper curve corresponds to the pair (32, 32), and the lower one to (1/8, 1/8). *Solid lines*: non-LTE models; *dotted lines*: LTE models. The models with the highest M_0 (with the highest IR, optical, and UV flux) have the largest He II Lyman jump, and consequently the lowest flux for $\nu > 2 \times 10^{16}$.

extreme for high-mass holes in the He II Lyman continuum, for which the LTE models predict virtually zero flux.

3.3.1. Effects of Changing the Viscosity Parameter α

In Figure 17 we compare the predicted spectra for disk models with $M_9 = 1$ for two values of the viscosity parameter α . Although the spectra exhibit some differences, the effect of different α is very small in the optical and UV region; the only appreciable differences are found in the He II Lyman continuum. This result is very encouraging because it shows that the effect of the ad hoc viscosity parameter α is rather small, and therefore the predicted spectra are not influenced significantly by this inherent uncertainty. Similar conclusions were reached in Paper II, albeit for a few representative annuli. The sense of the net effect is that larger α leads to a lower density and thus larger departures from LTE, which cause a somewhat higher flux in the He II Lyman continuum.

3.3.2. Schwarzschild Black Holes

Finally, we present several representative spectra for the case of a Schwarzschild black hole. Again, the full set of spectra is available upon request.

In Figure 18 we compare the predicted spectra for disk models with $M_9 = 1$, for the maximum rotating Kerr and Schwarzschild black holes. The total luminosity of the corresponding pairs of models is equal; the mass accretion rate is therefore a factor of 5.613 higher for the Schwarzschild case to adjust for the different efficiencies. The Kerr spectra tend to extend to higher frequencies for several reasons all arising from the fact that their disks extend in to smaller radii. As a result, the maximum effective temperature found in the disk is higher, and the relativistic effects strengthening the high frequency spectrum away from the axis are also greater.

This completes our presentation of the overall integrated spectra of our grid of models. We now address some of their observational implications.

3.4. Comparison with Other Models

We first compare the spectrum of an LTE model with that computed by Sincell & Krolik (1998). Figure 19 shows a comparison between one of their spectra and ours, computed for the same parameters. The agreement is satisfac-

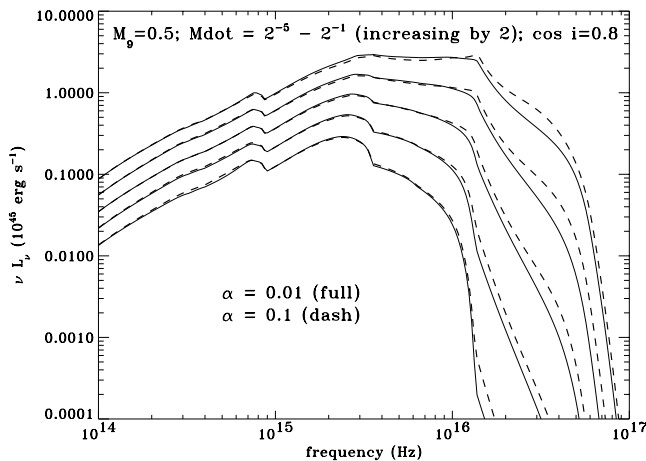


FIG. 17.—Comparison of predicted spectral energy distribution for models computed with $\alpha = 0.01$ (solid line) and with $\alpha = 0.1$ (dashed lines), for models with $M_9 = 1/2$ and various values of \dot{M} .

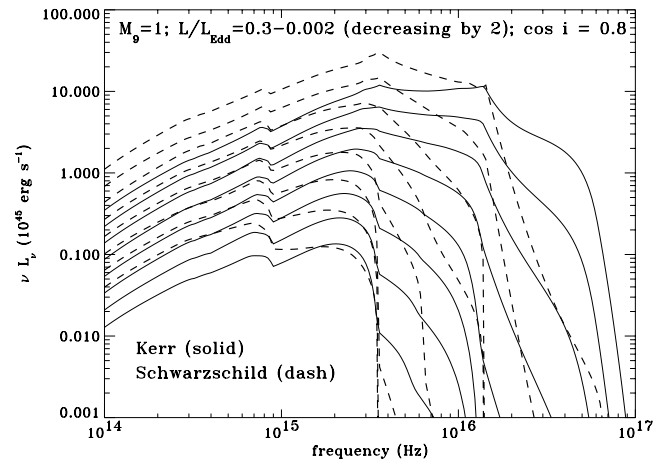


FIG. 18.—A comparison of predicted spectral energy distributions for the sequence of models for a maximum rotating Kerr black hole (solid line) and for a Schwarzschild black hole (dashed lines), for models with $M_9 = 1$ and various values of L/L_{Edd} . The values of the mass accretion rates are 2, 1, 1/2, and 1/4, etc., for the Kerr hole, and the corresponding values for the Schwarzschild hole are 5.613 times larger.

tory, as the spectra differ by at most 20% near the peak. The differences that do exist may be due to a number of factors, ranging from technical numerical contrasts in the methods to the detailed physical assumption made in both papers.

In Figure 20 we show a second comparison, this time to a Laor & Netzer (1989; Laor 1990) model, kindly supplied by A. Laor. We choose a model with $M_9 = 1$, $\dot{M} = 1 M_\odot \text{ yr}^{-1}$, (i.e., $L/L_{\text{Edd}} = 0.15$), $\alpha = 0.01$, and two values of $\cos i$: 0.8 and 0.2. We have integrated the local disk spectra out to a cutoff radius $r_{\text{out}}/r_g = 217.8$ to agree with Laor's value. The predicted spectra are generally similar, although there are several interesting differences. Our models produce larger flux in the immediate vicinity of the He II Lyman edge (due to non-LTE effects leading to an emission edge for the hottest annuli), but a lower flux for the highest frequencies (likely because Laor & Netzer take into account the effects of self-irradiation of the disk). Our models produce lower flux in the UV and optical regions, which is a consequence

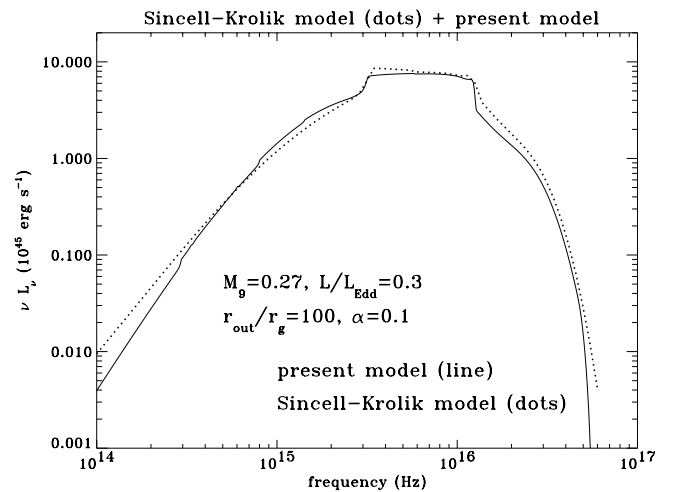


FIG. 19.—Comparison of an LTE disk model with Sincell & Krolik (1998). The solid line is our model; the dotted line is theirs. Model parameters are $M_9 = 0.27$, $a/M = 0$, $L/L_{\text{Edd}} = 0.3$, $r_{\text{out}} = 100r_g$, $\alpha = 0.1$, and the disk is viewed face-on.

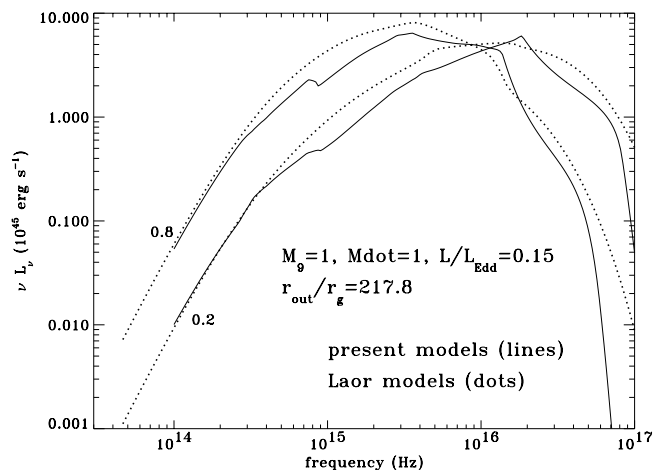


FIG. 20.—Comparison of a non-LTE disk model (solid curves) with a Laor & Netzer (1989; Laor 1990) model (dotted curves). Model parameters are $M_g = 1$, $L/L_{Edd} = 0.15$, $a/M = 0.998$, $r_{out} = 217.8r_g$, $\alpha = 0.01$, and $\cos i = 0.8$ and 0.2 .

of the different vertical structure and of non-LTE effects. Although the Laor & Netzer models do not simply assume local blackbody flux, Figure 7 is nevertheless quite indicative because it shows that local blackbodies also produce a significantly larger flux in the UV and optical region. At IR wavelengths both models coincide because both use local blackbody flux for the cool annuli.

3.5. Optical/Ultraviolet Colors

A common criticism of accretion disk models is that if they are to produce substantial ionizing photon flux, then they should have blue optical/ultraviolet colors. This is based on the long wavelength, low-frequency behavior of a blackbody disk, which has $F_\nu \propto \nu^\beta$, with $\beta = 1/3$. We address the issue of ionizing photon flux in § 3.8 below, but here we wish to point out that our disks have quite red optical/ultraviolet colors. Figure 21 shows the logarithmic spectral slope β as measured between 1450 and 5050 Å, where β is defined by the two corresponding frequencies by

$$\frac{F_{\nu_1}}{F_{\nu_2}} = \left(\frac{\nu_1}{\nu_2}\right)^\beta. \quad (5)$$

Our disk models have colors near the median value $\beta = -0.32$ for bright quasars (Francis et al. 1991). Indeed, even disks with local blackbody emission have such red colors for these accretion rates and masses (Koratkar & Blaes 1999). This is because the temperatures are cool enough that the 1450–5050 Å spectra are *not* in fact in the long-wavelength limit. Note that our model spectra can be somewhat bluer than blackbody disks, but they are still sufficiently red to explain the colors observed in bright quasars.

Figure 22 shows some representative Kerr disk models viewed at $i = 37^\circ$ compared to the Francis et al. (1991) composite quasar spectrum. The shorter wavelength composite spectrum of Zheng et al. (1997), scaled to match the Francis et al. spectrum at 1285 Å, is also shown. This latter composite is thought to be more trustworthy than the Francis et al. composite at wavelengths shorter than the Ly α /N v line because of corrections for intervening absorbers. The models were chosen to have the right color based on Figure

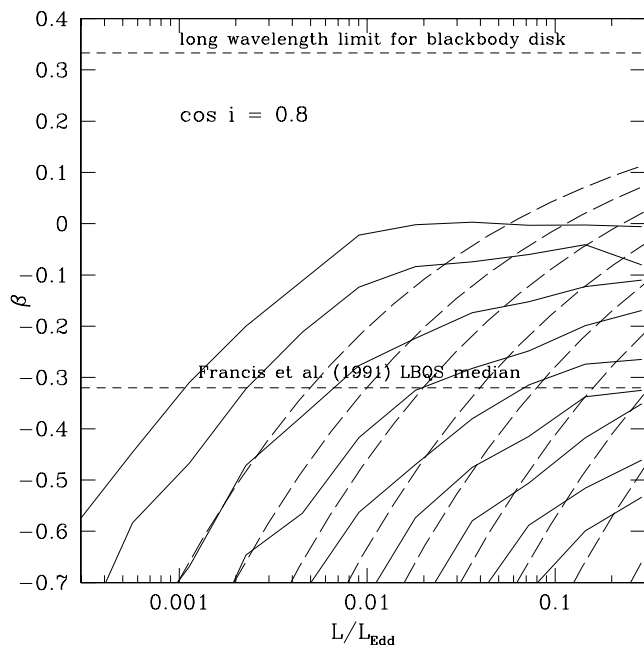


FIG. 21.—Optical/ultraviolet spectral slope between 1450 and 5050 Å for Kerr disk models with 37° viewing angle. Solid curves show our models with viscosity parameter $\alpha = 0.01$, while the long dashed curves show local blackbody models. From top to bottom, the curves are for the nine increasing black hole masses of our grid: $M_g = 1/8, 1/4, 1/2, 1, 2, 4, 8, 16,$ and 32 .

21, and then a least-squares fit was done to determine a single multiplicative normalization factor. The fit used supposedly line-free continuum windows of the Francis et al. (1991) composite spectrum, as defined by their Figure 7: 1283–1289 Å, 1321–1329 Å, 1455–1475 Å, 2196–2208 Å, 2236–2246 Å, 3024–3036 Å, 3928–3936 Å, 4035–4045 Å,

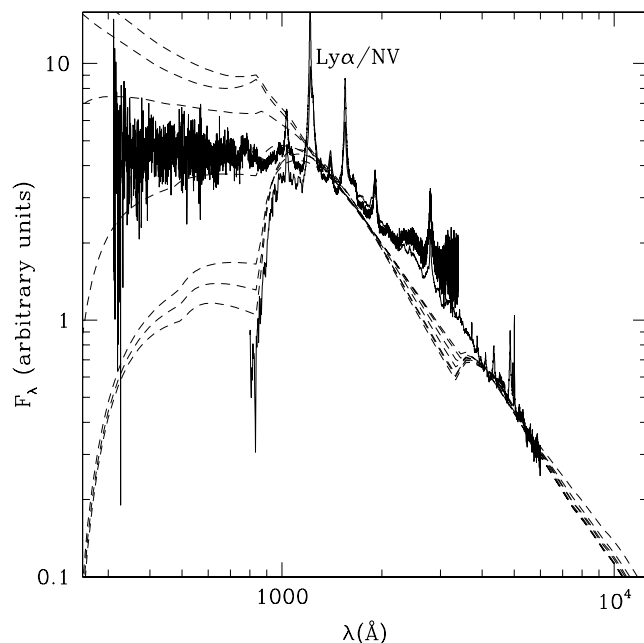


FIG. 22.—Representative fits of some Kerr disk models with viscosity parameter $\alpha = 0.01$ and $\cos i = 0.8$ to the Francis et al. (1991) composite quasar spectrum (solid line). The shorter wavelength composite spectrum of Zheng et al. (1997) is also shown (solid line with more noise). From top to bottom, the dashed lines correspond to models with $(M_g, M) = (8, 16), (4, 8), (2, 1), (1, 1/8), (0.5, 1/64), (1/4, 1/256),$ and $(1/8, 1/1024)$, respectively.

4150–4220 Å, and 5464–5476 Å. Note that the models shown have \dot{M}/M^2 ranging from 1/16 to 1/2, with the lower mass models having the smaller values of this quantity. This is consistent with the behavior shown in Figure 15: models with fixed \dot{M}/M^2 have slightly bluer optical/UV colors for decreasing black hole mass.

These fits demonstrate that, while it is easy to recover the overall red color of the Francis et al. (1991) composite spectrum, explaining the shorter wavelength far ultraviolet emission seen in the Zheng et al. (1997) composite is more problematic. Two of the models shown in Figure 22 do in fact bracket the Zheng et al. composite, but they turn over at the shortest wavelengths shown in the figure. This might be a problem in view of the fact that an extrapolation of the Zheng et al. composite joins up with the *ROSAT* soft X-ray composite of Laor et al. (1997), implying that there is no cutoff. However, it is also conceivable that some other choice of model parameters (disk inclination, black hole spin) might work better. Notice also that Zheng et al. suggested that in order to explain the Lyman continuum flux one has to invoke the presence of a Comptonizing corona with temperature about 4×10^8 K with optical depth of the order of unity. In any case, composite spectra made from many sources may of course be unphysical, but these fits probably give some indication of how our models will fare in explaining data from individual sources.

It is also noteworthy that the low-luminosity models shown in Figure 22 have rather strong spectral features in the region of the hydrogen Lyman limit, which are generally not observed in quasars. However, the models with the lowest luminosities are probably not representative of the quasars that make up the composite spectra. We now address this important issue of Lyman edges in AGN.

3.6. The Lyman Edge Region

Quasars and active galactic nuclei are observed to have almost no intrinsic spectral features near the hydrogen Lyman limit (e.g., Antonucci, Kinney, & Ford 1989; Koratkar, Kinney, & Bohlin 1992), and this has been a long-standing problem with accretion disk models (e.g., Krolik 1999a; Koratkar & Blaes 1999). To quantify the strength of Lyman edge features in our model disk spectra, we calculate the relative change in flux at ± 50 Å across the edge according to

$$\frac{\Delta F_\lambda}{F_\lambda} \equiv \frac{F_{962 \text{ \AA}} - F_{862 \text{ \AA}}}{\min(F_{962 \text{ \AA}}, F_{862 \text{ \AA}})}. \quad (6)$$

Hence $\Delta F_\lambda/F_\lambda$ is positive for an absorption edge and negative for an emission edge. Figure 23 shows the variation of this quantity with accretion luminosity and disk inclination angle for all our models around a $M_\odot = 1$ Kerr hole. Figure 24 shows the same thing but for a fixed inclination angle of 37° and varying black hole masses. As was already apparent from the overall spectra shown in previous sections, substantial Lyman absorption edges are present in all our low-luminosity disk models at modest, near face-on viewing angles. However, high-luminosity models have greatly reduced edges, particularly for the lower mass black holes. Because of their lower effective temperatures, higher mass black holes require higher Eddington ratios before the absorption edges are removed.

It is important to emphasize that the absorption and emission edges can be smeared out by the varying Doppler

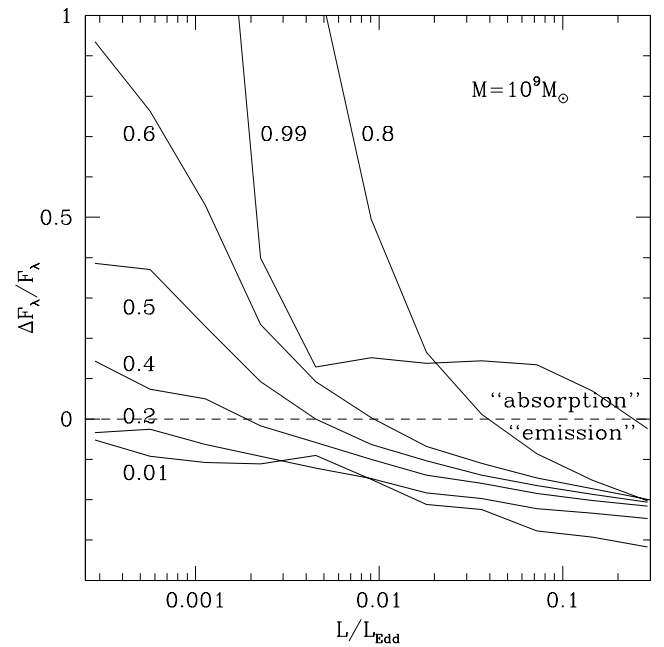


FIG. 23.—Measure of the hydrogen Lyman edge strength as a function of accretion luminosity, in units of the Eddington luminosity, for $\alpha = 0.01$ accretion disks around Kerr holes with mass $M_\odot = 1$. The curves are labeled with the value of $\cos i$.

shifts and gravitational redshifts in the accretion flow around the black hole when the viewing direction is at least somewhat off-axis. This is illustrated in Figures 25 and 26, which show the actual spectral energy distributions of some of our models in the Lyman limit region. The high-luminosity models, which are probably most relevant for observed quasars, show very little in terms of sharp changes in flux, and our edge strength parameter shown in Figures 23 and 24 really reflects an overall spectral slope, not an emission edge, in this wavelength region. These high-

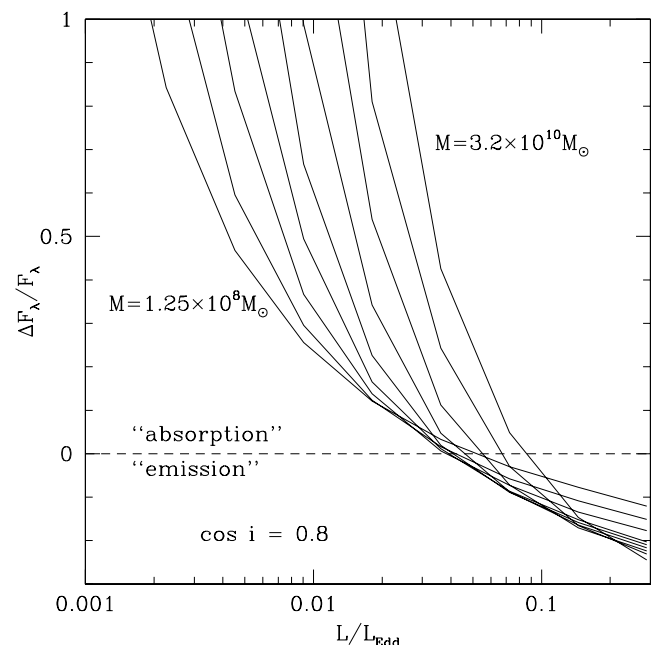


FIG. 24.—Same as Fig. 23, but for fixed inclination angle of 37° and varying Kerr black hole mass.

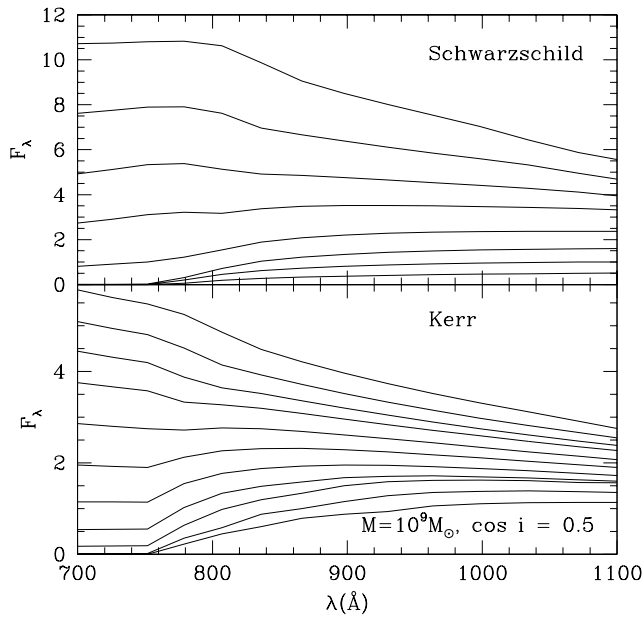


FIG. 25.—Spectral energy distributions in wavelength near the hydrogen Lyman limit for fixed Schwarzschild and Kerr black hole mass of $M_9 = 1$ and viewing angle of 60° . From bottom to top, the curves represent accretion rates of 2^{-9} , 2^{-8} , ..., 2^0 , and $2^1 M_\odot \text{ yr}^{-1}$, respectively, except in the Schwarzschild case where we have dropped the three lowest accretion rates. (The $2^{-6} M_\odot \text{ yr}^{-1}$ Kerr curve is the same as the curve with the strongest Lyman absorption edge shown in Fig. 22.) Each curve has had its flux multiplied by a different constant factor in order to maximize clarity with all the curves on the same plot. All models shown here have a viscosity parameter $\alpha = 0.01$.

luminosity models are still capable of explaining the observed red colors of quasars, as shown in Figures 21 and 22.

Reduction of the Lyman edge feature is caused both by relativity and by summing over emission and absorption edges from the individual annuli at different radii. Only relativity (i.e., Doppler shifts) can smear out a flux discontinuity, however.

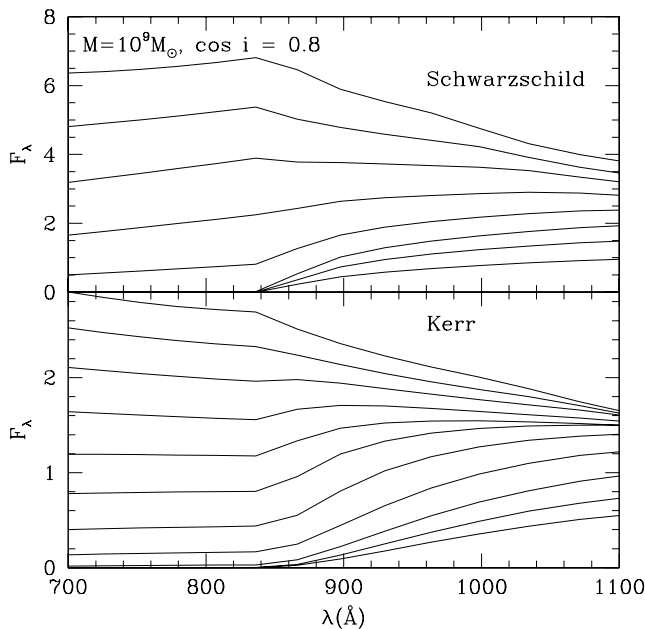


FIG. 26.—Same as Fig. 25, but for viewing angle of 37°

Instead, the edges are simply blueshifted or redshifted away from 912 \AA .

Sharp changes in slope are present in the low-luminosity Kerr spectra near $\approx 750 \text{ \AA}$ for $\cos i = 0.5$, and in most of the spectra near $\approx 840 \text{ \AA}$ for $\cos i = 0.8$. In both cases these are at substantially shorter wavelengths than the Lyman limit because of Doppler blueshifts, but they might nevertheless be observable in quasar spectra. From our models, we have calculated the maximum local change in logarithmic slope in the region $812\text{--}1012 \text{ \AA}$, and the results are illustrated in Figure 27 for a viewing angle of 37° . We choose a sign convention such that a positive value of the slope change indicates a spectrum that becomes steeper as the frequency increases, i.e., positive slope change is associated with absorption at the edge. All models display a similar behavior at this viewing angle, so we only discuss the $M = 10^9 M_\odot$ case in detail (see Fig. 26 and the bold curve in Fig. 27). At both low and high accretion rates, the maximum slope change occurs at $\approx 840 \text{ \AA}$ for this black hole mass. As the accretion rate diminishes, $\Delta(d \ln F_\lambda / d \ln \lambda)$ grows, reflecting an increasingly stronger smeared absorption edge. The reverse is true at high accretion rates. At intermediate accretion rates, the maximum slope discontinuity shifts to $\approx 900 \text{ \AA}$, where the spectra change from positive to negative slopes, reflecting a slight maximum in the flux around this wavelength for these models.

In conclusion, the disk-integrated theoretical spectra for high Eddington ratio (L/L_{Edd}) disks do not show significant

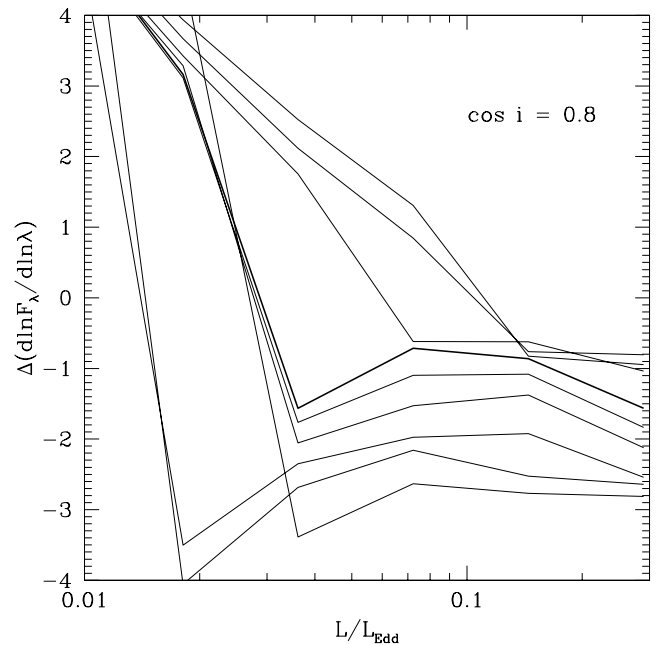


FIG. 27.—Maximum local change in logarithmic slope in $812\text{--}1012 \text{ \AA}$ region, as a function of accretion rate, for $\alpha = 0.01$ accretion disks viewed at 37° around Kerr holes of masses $(2^{-3}, 2^{-2}, \dots, 2^4, 2^5) \times 10^9 M_\odot$. The bold curve is the $M = 10^9 M_\odot$ case illustrated in the bottom half of Fig. 26.

features at the Lyman edge at 912 \AA , for both Kerr and Schwarzschild black holes. The only associated feature is a change of the slope of the Lyman continuum, blueshifted by $\sim 100\text{--}200 \text{ \AA}$, depending on the inclination, mass, and to some extent on the black hole spin. It is likely that even this feature will be affected by additional physics, particularly metal line blanketing, which we will address in a future paper.

3.7. Polarization

In addition to computing spectra, we have also calculated the polarization in our complete grid of models, and this information is also available on request. Once again, no ad hoc assumptions are made here: the polarization is computed exactly in the radiative transfer calculation. In order to keep the parameter space as simple as possible, we do not include the effects of Faraday rotation by magnetic fields in the photosphere of the accretion disk, which can be important in modifying the polarization signature (e.g., Agol, Blaes, & Ionescu-Zanetti 1998).

Figure 28 shows the degree and position angle of the polarization for various inclination angles for our $\alpha = 0.01$, $\dot{M} = 1 M_{\odot} \text{ yr}^{-1}$ disk models around a $M = 10^9 M_{\odot}$ Kerr hole. These results are quite similar to those of Laor, Netzer, & Piran (1990). In particular, the plane of polarization is parallel to the disk plane at optical/UV frequencies but rotates at higher frequencies due to general relativistic effects. Our predicted polarizations are higher than those of Laor et al. (1990), and our polarization generally dips redward and rises blueward of each continuum edge (see especially the hydrogen Balmer edge and He II Lyman edge). These differences are due largely to our more careful treatment of the vertical structure, the radiation field anisotropy, and the overall effects of absorption opacity.

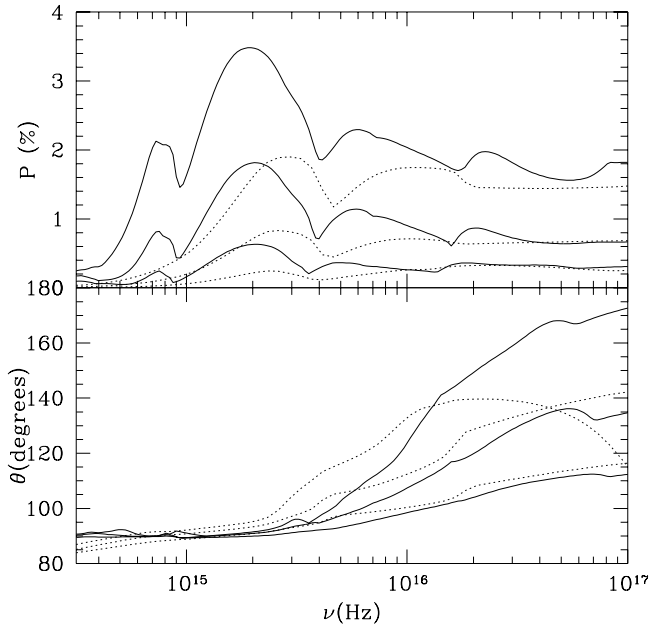


FIG. 28.—Polarization degree and position angle (θ) for $\alpha = 0.01$, $\dot{M} = 1 M_{\odot} \text{ yr}^{-1}$ disks around a $M = 10^9 M_{\odot}$ Kerr hole, for different viewing angles. Solid curves correspond to our models, while dotted curves are those of Laor et al. (1990). From top to bottom at high frequencies in the degree of polarization figure, the different curves correspond to $\cos i = 0.2, 0.5$, and 0.8 , respectively. This order is reversed (i.e., bottom to top) in the position angle figure. A position angle of $\theta = 90^\circ$ corresponds to the plane of polarization being parallel to the disk plane.

Polarization near the Lyman limit of hydrogen has produced considerable recent interest due to the observation of steep rises in some quasars (Impey et al. 1995; Koratkar et al. 1995; Koratkar et al. 1998). For illustration purposes, we show the degree of polarization at a viewing angle of 60° predicted by our models for $M_{\odot} = 1$ black holes in Figure 29. This figure should be compared to Figure 25, which shows the corresponding spectra. Cooler disk models generally produce large polarizations, even larger than that for a pure electron scattering atmosphere (2.25% at this viewing angle, Chandrasekhar 1960, p. 248). The reason for this is the enhanced anisotropy (limb darkening) of the radiation field due to vertical thermal source function gradients (Blaes & Agol 1996). However, steep rises in polarization, and a steep rise in polarized flux as observed in PG 1630+377 (Koratkar et al. 1995), are not produced by our models. This is partly due to the smearing and rotation of the plane of polarization by the relativistic transfer function (cf. Shields, Wobus, & Husfeld 1998).

The optical/UV polarization shown in Figure 28 (in degree, position angle, and wavelength dependence) is generally not observed in AGN and quasars (Berriman et al. 1990; Antonucci et al. 1996). Once again, it is likely that the polarization of the radiation field will be affected by additional physics. In addition to Faraday rotation (which usually suppresses polarization), the additional absorption opacity from metal line blanketing in this region of the spectrum will probably reduce the polarization. Dust and electron scattering at larger distances from the continuum source can also modify the polarization signature (Kartje 1995).

3.8. Ionizing Continua

The radiation from accretion disks is often thought to supply most of the photoionizing continuum for the broad-

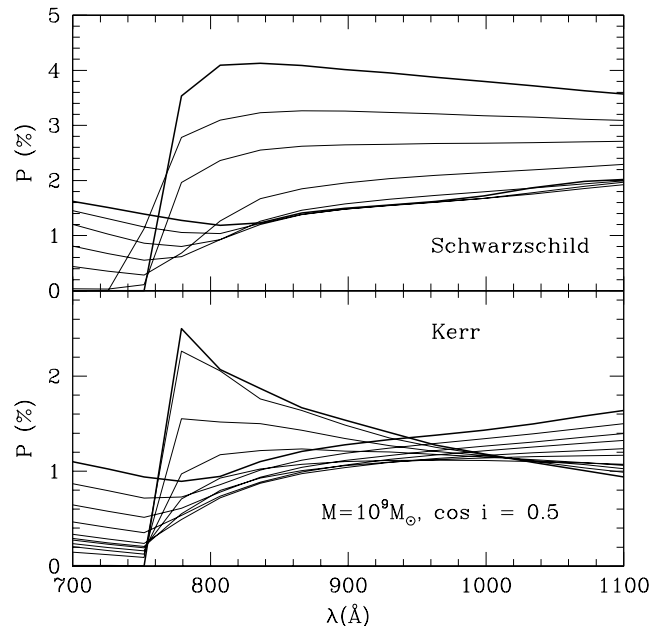


FIG. 29.—Degree of polarization in the hydrogen Lyman limit region for disks around $10^9 M_{\odot}$ Schwarzschild and Kerr black holes and a viewing angle of 60° . The models shown here are the same as those plotted in Fig. 25, with the bold curves in each plot representing the highest and lowest accretion rates. (The lowest accretion rate gives the highest polarization around 800 \AA .)

and narrow-line regions of AGN. In view of this important application, we present the number of photons in the He I and He II ionizing continua for disks with a range of accretion rates and inclination angles around $10^9 M_\odot$ Kerr holes in Figures 30 and 31. For comparison, we also show the ionizing continua for the corresponding models with local blackbody emission. For this particular black hole mass, our models generally predict somewhat fewer ionizing photons in the hydrogen Lyman continuum than the corre-

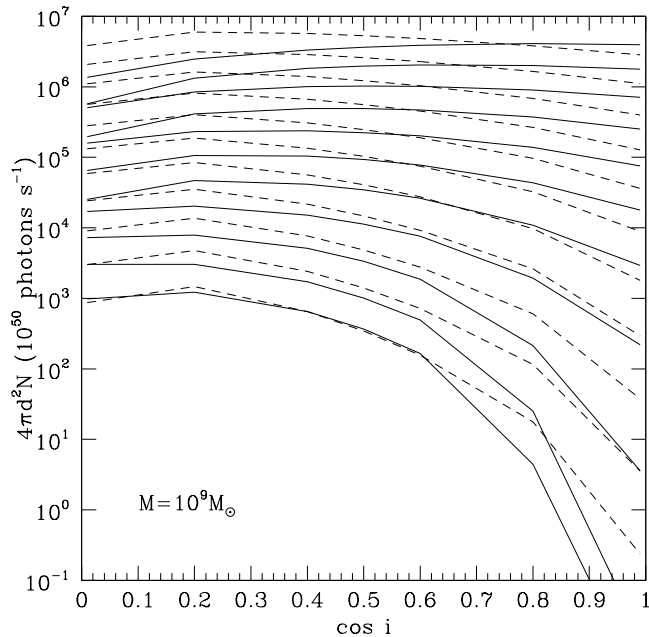


FIG. 30.—Hydrogen Lyman continuum photon flux (times $4\pi d^2$, where d is the distance to the quasar) for $\alpha = 0.01$ disks around a $M_\odot = 1$ Kerr black hole, as a function of viewing angle i . Solid and dashed curves correspond to our non-LTE models and local blackbody disks, respectively. From top to bottom, the curves correspond to accretion rates of $2^1, 2^0, \dots, 2^{-8}, 2^{-9} M_\odot \text{ yr}^{-1}$, respectively.

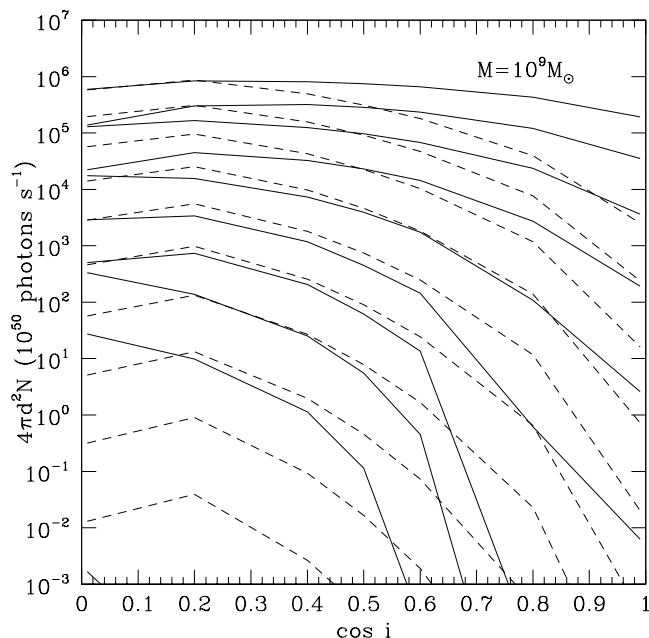


FIG. 31.—Same as Fig. 30, but for the He II Lyman continuum. The lowest accretion rates are off the bottom of the figure.

sponding blackbody disks. The exception is for near face-on disks at high luminosities. The reason is that at each annulus in the disk, our models generally have fewer low-energy photons and more high-energy photons compared to a blackbody at the same effective temperature (see Fig. 7 and § 3.1 above). This can reduce the hydrogen Lyman continuum, while at the same time increasing the He II Lyman continuum. Indeed, Figure 31 shows that, except at low luminosities, our disk models generally produce more He II Lyman continuum photons than local blackbody disks. The reason for the dearth of photons at low luminosities compared to blackbody models is the strong absorption edges present in these models.

Note that the hydrogen Lyman continuum is limb-darkened at high accretion rates, peaks at intermediate viewing angles at moderate accretion rates, and is extremely limb-brightened at low accretion rates (due to the high Doppler shifts overcoming the intrinsic absorption edges). The He II Lyman continuum is also limb brightened at all but the highest accretion rates, where it peaks at intermediate viewing angles. These intrinsic anisotropies in the ionizing continuum produced by the disk may have important implications for photoionization models of the broad-line region of AGNs (cf. the much simpler anisotropy model of Netzer 1987) and for the statistics of AGN samples (e.g., Krolik & Voit 1998).

4. CONCLUSIONS

We have presented a grid of AGN disk models for a wide range of basic parameters, the black hole mass and the mass accretion rate, and for two values of the viscosity parameter α (0.01 and 0.1), and two values of the black hole angular momentum: maximum rotation Kerr black hole with $a/M = 0.998$, and Schwarzschild black hole with $a/M = 0$.

The basic aim of the present study was to construct a benchmark grid of models, based on simple, “classical” approximations, to which all our future, more elaborate models will be compared. The most important physical approximations that define the classical model are the following:

1. The energy is generated by turbulent viscous dissipation, with the vertically averaged viscosity described through the Shakura-Sunyaev parameter α .
2. The vertical dependence of kinematic viscosity is described through a two-step power law in the column mass.
3. Convection and conduction are neglected.
4. No external irradiation or self-irradiation of the disk is considered.
5. Electron scattering is treated as coherent (Thomson) scattering, i.e., the effects of Comptonization are neglected.
6. Thermal opacity and emissivity of H and He only are included here, i.e., the effects of metals are neglected.
7. Effects of line opacity are neglected.

The underlying assumption, not listed here, is that the one-dimensional approach is appropriate, i.e., that the disk may be described as a set of mutually noninteracting, concentric annuli.

What is, however, treated exactly in this study, is the simultaneous solution of all the structural equations, without making any approximations concerning the behavior of the radiation intensity. Likewise, no a priori assumptions about atomic level populations (e.g., LTE) are made.

The local electron temperature and density, mass density, and atomic level populations, are determined self-consistently with the radiation field. Once the local spectra of all annuli are computed, the spectrum of the full disk is found by integrating the emergent intensity over the disk surface using our relativistic transfer function code.

We can summarize some of the overall spectral features of our benchmark grid as follows. Compared to multi-temperature blackbody accretion disk models, our spectra generally have lower fluxes at low frequencies and higher fluxes at high frequencies. This difference is amplified further by relativistic effects, which are strongest for edge-on disks in Kerr spacetimes. Disks with different accretion rates around different mass black holes do *not* exhibit the same spectral energy distribution even if they have the same effective temperature distribution. Spectral slopes in the optical/UV region are significantly redder than the canonical $F_\nu \propto \nu^{1/3}$ low-frequency accretion disk spectrum. Non-LTE effects are important in all but the highest density disks, enhancing the He II Lyman continuum and generally reducing the strength of features near the He I Lyman limit. H I Lyman edge discontinuities are only present in the cooler, low-luminosity disk models. High Eddington ratio models exhibit no discontinuities, but they do show sharp changes in spectral slope, albeit at wavelengths substantially blueshifted from 912 Å. We stress again that by neglecting convection, the “cool” models ($T_{\text{eff}} < 9000$ K) may be significantly altered; therefore the predicted optical and IR continuum flux (and, in particular, the Balmer edge region) should be used with caution. Finally, our models show substantial wavelength dependent optical/UV polarization which is parallel to the disk plane, a result which is likely to be modified by the effects of Faraday rotation and additional sources of opacity, both of which can suppress this polarization.

In future papers of this series, we will systematically relax more and more of the classical assumptions listed above. Among these, relaxing assumptions (6) and (7) is straightforward, since our computer program TLUSDISK is fully

capable of handling these situations. The only concern is that generating such models will require much more computer time than required for the present models. Also, one has to collect a large amount of atomic data, but we will profit enormously from already existing collections made for the purposes of modeling stellar atmospheres, or from data being included in current photoionization codes. Relaxing approximation (5) is less straightforward, but we have recently solved the problem and implemented Comptonization in TLUSDISK. Also, approximation (4) may in principle be easily relaxed by adjusting the surface boundary conditions of each annulus.

However, relaxing assumptions (1)–(3) is much more difficult. Here, we have to rely on detailed magnetohydrodynamic simulations to guide us in how to describe convection, and how to choose the most appropriate parameterization of viscosity. Nevertheless, even before such simulations are available, we can investigate phenomenologically the impact of a dissipation rate that varies with altitude within the disk. The existence of disk coronae suggest, for example, that the heating rate may increase with height, leading to a possible temperature inversion in the upper layers of disk atmospheres.

Besides this purely theoretical motivation for improving disk models we will also use the present grid of models to analyze a large volume of observed quasar spectra. Such a study will bring interesting results whether or not the models actually fit the data. If they do, this will be a strong argument in support of the accretion disk hypothesis, and of the adequacy of our theoretical description of accretion disks. If not, such a study will provide us with important clues as to which aspects of the theoretical description should be improved, and/or what other observational constraints will be needed in the future to settle these questions.

We thank Ari Laor for providing us with his spectral models for comparison with those presented here. This work was supported in part by NASA grant NAG 5-7075.

APPENDIX A

DENSITY STRUCTURE OF THE DISK

We consider here some details of the density structure in the case of a radiation pressure–supported disk, without assuming that the gas pressure is totally negligible.

We write the vertical hydrostatic equilibrium equation as (see Paper II for details of the formulation)

$$\frac{dP_{\text{rad}}}{dz} + \frac{dP_{\text{gas}}}{dz} = -Q\rho z, \quad (\text{A1})$$

where P_{rad} and P_{gas} are the radiation and gas pressure, respectively; ρ is the mass density; z is the vertical distance from the disk midplane; and $Q = (GM/r^3)(C/B)$ [in the notation of Paper II; in the notation of Krolik 1999a, $C/B = R_z(r)$], where B , C , and $R_z(r)$ are the appropriate relativistic corrections.

The radiation pressure gradient can be written (Paper II; Krolik 1999a)

$$\frac{dP_{\text{rad}}}{dz} = -\frac{\rho\chi_{\text{H}}}{c} F_{\text{rad}}, \quad (\text{A2})$$

where F_{rad} is the total (frequency-integrated) radiation flux, and χ_{H} is the flux-mean opacity. For most applications, the flux-mean opacity is well approximated by the Rosseland-mean opacity, κ_{R} . We consider here the case where the local opacity is fully dominated by electron scattering, in which case κ_{R} is constant and roughly equal to 0.34. (In fact, it is not exactly constant because it depends on the degree of ionization—see Paper II; however, we neglect this small effect here.) Further, we

introduce (Krolik 1999a)

$$F_{\text{rad}}(z) = F_{\text{rad}}^0(z)f(z) \equiv \sigma_{\text{B}} T_{\text{eff}}^4 f(z), \quad (\text{A3})$$

where F_{rad}^0 is the total radiation flux at the surface, which is expressed through the effective temperature.

We express the gas pressure through the sound speed, c_s , as $P_{\text{gas}} = c_s^2 \rho$. The sound speed is given by

$$c_s^2 = \frac{k}{\mu m_{\text{H}}} \frac{N}{N - n_e} T, \quad (\text{A4})$$

where k and m_{H} are the Boltzmann constant and the mass of the hydrogen atom, respectively; μ is the mean molecular weight (i.e., the mean mass of a heavy particle per hydrogen atom; in our case of a H-He atmosphere with a solar helium abundance $\mu = 1.4/1.1 = 1.27$); N is the total particle number density, and n_e is the electron density. The sound speed thus depends primarily on the temperature, and partly also on the degree of ionization [via the term $N/(N - n_e)$, which varies from 1 (for a neutral medium) to 2.1 (for a fully ionized solar-composition H-He plasma)].

Substituting equations (A2), (A3), and (A4) into (A1), we obtain

$$\frac{1}{Q} \frac{dc_s^2}{dz} + \frac{c_s^2}{\rho Q} \frac{d\rho}{dz} = H_r f(z) - z, \quad (\text{A5})$$

where we introduce the radiation-pressure scale height, H_r , as

$$H_r \equiv \frac{\kappa_{\text{R}} F_{\text{rad}}^0}{cQ} = \frac{\kappa_{\text{R}} \sigma_{\text{B}} T_{\text{eff}}^4}{cQ}, \quad (\text{A6})$$

which has the meaning of the disk height in the case of negligible gas pressure (see Paper II and Krolik 1999a).

We shall consider two cases, (1) the gas pressure is completely negligible, and (2) the gas pressure is taken into account, although it is still smaller than the radiation pressure.

In the former case, we take $P_{\text{gas}} = 0$, i.e., $c_s = 0$, and thus the left-hand side of equation (A5) is zero. We are left with

$$H_r f(z) - z = 0. \quad (\text{A7})$$

At the surface, $f(z_0) = 1$ regardless of the dissipation law, and therefore $z_0 = H_r$, so the disk height is exactly equal to the radiation-pressure scale height. However, the density cancels out exactly because both the gravity force and radiation force are linearly proportional to density (e.g., Krolik 1999a), so the density is undetermined by the hydrostatic equilibrium equation. In usual treatments of the radiation pressure-supported disk, equation (A7) is assumed to hold everywhere in the disk, from which it follows that $f(z) = z/H_r$. In our approach, however, we assume that f is a known function of the column mass, m . In the case of constant kinematic viscosity (i.e., the dissipation rate proportional to density), we have (see Paper II), $f = m/m_0$, where m_0 is the column mass at the midplane, $m_0 = \Sigma/2$. This gives a linear relation between z and m , and since $\rho = -dm/dz$, we obtain $\rho(z) = \text{const} = \rho_0$ in the region of constant dissipation (99% of the total column mass of the disk in our models). In our numerical procedure, we in fact solve equation (A5) exactly, without assuming that the left-hand side is negligible, and with f given as a known function of m (although not of z , because z is one of the state parameters to be solved as a function of m).

To be able to write down a simple analytic solution in the case of nonnegligible gas pressure, we approximate the function $f(z)$ as

$$f(z) = \begin{cases} z/H_0, & \text{for } z < H_0, \\ 1, & \text{for } z \geq H_0. \end{cases} \quad (\text{A8})$$

In other words, we assume that the radiation flux linearly increases with z until a certain height H_0 , and then remains constant. Such a behavior is roughly observed in the numerical simulations. Since close to the midplane $z/H_0 = 1 - m/m_0$, so that $\rho_0 = -(dm/dz)_{z=0} = m_0/H_0$. Therefore, $H_0 = m_0/\rho_0$. Within the present analytical model, H_0 , and thus ρ_0 are quantities to be determined by the constraint of total column density (see below). We write

$$\frac{c_s^2}{Q} = \frac{c_s^2(z=0)}{Q} q(z) \equiv \frac{H_g^2}{2} q(z), \quad (\text{A9})$$

where H_g has the meaning of the gas-pressure scale height corresponding to the midplane conditions (temperature and degree of ionization), and $q(z)$ is a correction parameter that accounts for a dependence of c_s on z . The reason why H_g is called the gas-pressure scale height is that in the case of negligible radiation force [i.e., $f(z) \rightarrow 0$ everywhere], the solution of equation (A5) is given by

$$\rho(z) \rightarrow \rho_0 \exp[-(z/H_g)^2], \quad (\text{A10})$$

where $\rho_0 \equiv \rho(z=0)$ is the density at the midplane.

In the following, we neglect the dependence of sound speed on height, i.e., we assume $q(z) = 1$. One can derive appropriate analytical expressions even for a more realistic case at the expense of complicating the analytical formulas considerably, but the present approximation is satisfactory from the point of view of describing the basic physical picture. A similar analysis was

already presented by Hubeny (1990). Equation (A5) then reads, using equation (A9),

$$\frac{1}{\rho} \frac{d\rho}{dz} = \left(\frac{H_r}{H_0} - 1 \right) \frac{2z}{H_g^2} \quad \text{for } z < H_0, \quad (\text{A11})$$

$$\frac{1}{\rho} \frac{d\rho}{dz} = (H_r - z) \frac{2}{H_g^2} \quad \text{for } z \geq H_0, \quad (\text{A12})$$

which has the solution

$$\rho(z) = \rho_0 \exp \left[- \left(1 - \frac{H_r}{H_0} \right) \left(\frac{z}{H_g} \right)^2 \right] \quad \text{for } z < H_0, \quad (\text{A13})$$

and

$$\rho(z) = \rho_0 \exp \left[- \left(\frac{z - H_r}{H_g} \right)^2 \right] \exp \left(- \frac{H_r}{H_g} \frac{H_0 - H_r}{H_g} \right) \quad \text{for } z \geq H_0. \quad (\text{A14})$$

The scale height H_0 is now determined from the condition $\int_0^\infty \rho(z) dz = m_0$. Substituting equations (A13) and (A14), we obtain after some algebra

$$(2/\sqrt{\pi})h_0 = \sqrt{h_0/\delta_0} \operatorname{erf}(\sqrt{h_0 \delta_0}) + \exp(-h_r \delta_0) \operatorname{erfc}(\delta_0), \quad (\text{A15})$$

where

$$h_0 \equiv H_0/H_g, \quad h_r \equiv H_r/H_g, \quad (\text{A16})$$

and

$$\delta_0 = h_0 - h_r, \quad (\text{A17})$$

where the error function $\operatorname{erf}(x)$ is defined by $\operatorname{erf}(x) \equiv (2/\sqrt{\pi}) \int_0^x \exp(-t^2) dt$, and the complementary error function is defined by $\operatorname{erfc}(x) \equiv (2/\sqrt{\pi}) \int_x^\infty \exp(-t^2) dt = 1 - \operatorname{erf}(x)$. Equation (A15) is a transcendental equation for h_0 ; however an approximate solution is found to be

$$h_0 \approx h_r + 1/h_r. \quad (\text{A18})$$

If $h_r \gg 1$ (i.e., $H_r \gg H_g$), one obtains $h_0 \approx h_r$, i.e., $H_0 \approx H_r$, and thus $\rho(z) \approx \rho_0$ for $z < H_r$; i.e., one recovers the solution for negligible gas pressure. If, however, H_g is not completely negligible with respect to H_r , we obtain $H_0 > H_r$, and density falls off exponentially with increasing height even in the midplane layer, with a scale height $H_g/(1 - H_r/H_0)^{1/2}$ (see eq. [A13]).

From the expression for the respective scale heights we see that H_r is weakly dependent on r ($H_r \propto D/C$, so it depends on radial distance only through the relativistic corrections), while $H_g \propto (T_0/Q)^{1/2}$ where T_0 is the temperature at the midplane. The latter scales as $T_0 \propto m_0^{1/4} T_{\text{eff}} \propto r^{-3/8}$, and since $Q \propto r^{-3}$, we obtain finally $H_g \propto r^{21/16}$, i.e., it increases rapidly with radial distance. For the models displayed in Figure 3 we have, e.g., at $r/r_g = 5$ (which is well in the domain of complete dominance of radiation pressure), $H_r = 2.63 \times 10^{13}$ cm, and $H_g = 5.52 \times 10^{11}$ cm, i.e., $h_r \approx 48$. We thus have $H_0 \approx H_r$, which is indeed verified by the numerical model. The last (coolest) model displayed there corresponds to $r/r_g = 90$, and we have $H_r = 6.42 \times 10^{13}$ cm, and $H_g = 2.67 \times 10^{13}$ cm, i.e., $h_r \approx 2.4$. The correction $1/h_r$ to h_0 is no longer negligible; we obtain $h_0 \approx 2.8$, i.e., $H_0 \approx 7 \times 10^{13}$ cm (the exact value following from the numerical model is $H_0 = 7.7 \times 10^{13}$ cm), and the density should show an $\exp[-(z/H)^2]$ decay with z with $H \approx 9.3 \times 10^{13}$ cm. This is indeed roughly consistent with the numerical model.

REFERENCES

- Agol, E. 1997, Ph.D. thesis, Univ. California, Santa Barbara
 Agol, E., Blaes, O., & Ionescu-Zanetti, C. 1998, MNRAS, 293, 1
 Agol, E., & Krolik, J. H. 2000, ApJ, 528, 161
 Antonucci, R., Geller, R., Goodrich, R. W., & Miller, J. S. 1996, ApJ, 472, 502
 Antonucci, R., Kinney, A. L., & Ford, H. C. 1989, ApJ, 342, 64
 Balbus, S. A. 1999, ApJ, submitted (astro-ph/9906315)
 Balbus, S. A., & Hawley, J. F. 1998, Rev. Mod. Phys., 70, 1
 Berriman, G., Schmidt, G. D., West, S. C., & Stockman, H. S. 1990, ApJS, 74, 869
 Bisnovatyi-Kogan, G. S., & Blinnikov, S. I. 1977, A&A, 59, 111
 Blaes, O., & Agol, E. 1996, ApJ, 469, L41
 Chandrasekhar, S. 1960, Radiative Transfer (New York: Dover)
 Cunningham, C. T. 1975, ApJ, 202, 788
 Dörner, T., Riffert, H., Staubert, R., & Ruder, H. 1996, A&A, 311, 69
 Francis, P. J., Hewett, P. C., Foltz, C. B., Chaffee, F. H., Weymann, R. J., & Morris, S. L. 1991, ApJ, 373, 465
 Gammie, C. F. 1999, ApJ, submitted
 Hubeny, I. 1988, Comput. Phys. Commun., 52, 103
 ———. 1990, ApJ, 351, 632
 ———. 1992, in The Atmospheres of Early-Type Stars, ed. U. Heber and C. J. Jeffery (Berlin: Springer), 377
 Hubeny, I., & Hubeny, V. 1997, ApJ, 484, L37 (Paper I)
 ———. 1998a, ApJ, 505, 558 (Paper II)
 Hubeny, I., & Hubeny, V. 1998b, in AIP Conf. Proc. 431, Accretion Processes in Astrophysical Systems: Some Like it Hot!, ed. S. S. Holt & T. R. Kallman (Woodbury: AIP), 171
 Hubeny, I., Hummer, D. G., & Lanz, T. 1994, A&A, 282, 157
 Hubeny, I., & Lanz, T. 1992, A&A, 262, 501
 ———. 1995, ApJ, 439, 875
 Impey, C. D., Malkan, M. A., Webb, W., & Petry, C. G. 1995, ApJ, 440, 80
 Kartje, J. F. 1995, ApJ, 452, 565
 Kolykhalov, P. I., & Sunyaev, R. A. 1984, Adv. Space Res., 3, 249
 Koratkar, A., Antonucci, R. R. J., Goodrich, R. W., Bushouse, H., & Kinney, A. L. 1995, ApJ, 450, 501
 Koratkar, A., Antonucci, R. R. J., Goodrich, R. W., & Storrs, A. 1998, ApJ, 503, 599
 Koratkar, A., & Blaes, O. 1999, PASP, 111, 1
 Koratkar, A. P., Kinney, A. L., & Bohlin, R. C. 1992, ApJ, 400, 435
 Krolik, J. H. 1999a, Active Galactic Nuclei (Princeton: Princeton Univ. Press)
 ———. 1999b, ApJ, 515, L73
 Krolik, J. H., & Voit, G. M. 1998, ApJ, 497, L5
 Laor, A. 1990, MNRAS, 246, 369
 Laor, A., Fiore, F., Elvis, M., Wilkes, B. J., & McDowell, J. C. 1997, ApJ, 477, 93
 Laor, A., & Netzer, H. 1989, MNRAS, 238, 897
 Laor, A., Netzer, H., & Piran, T. 1990, MNRAS, 242, 560

- Netzer, H. 1987, *MNRAS*, 225, 55
Page, D., & Thorne, K. S. 1974, *ApJ*, 191, 499
Ross, R. R., Fabian, A. C., & Mineshige, S. 1992, *MNRAS*, 258, 189
Shakura, N. I., & Sunyaev, R. A. 1973, *A&A*, 24, 337
Shakura, N. I., Sunyaev, R. A., & Zilitinkevich, S. S. 1978, *A&A*, 62, 179
Shapiro, S. L., & Teukolsky, S. A. 1983, *Black Holes, White Dwarfs, and Neutron Stars* (New York: Wiley)
Shields, G. A., & Coleman, H. H. 1994, in *Theory of Accretion Disks*, ed. W. J. Duschl et al. (NATO ASI Ser. C, 417; Dordrecht: Kluwer), 223
Shields, G. A., Wobus, L., & Husfeld, D. 1998, *ApJ*, 496, 743
Shimura, T., & Takahara, F. 1993, *ApJ*, 419, 78
———. 1995, *ApJ*, 440, 610
Sincell, M. W., & Krolik, J. H. 1998, *ApJ*, 496, 737
Störzer, H., Hauschildt, P. H., & Allard, F. 1994, *ApJ*, 437, L91
Sun, W.-H., & Malkan, M. A. 1989, *ApJ*, 346, 68
Zheng, W., Kriss, G. A., Telfer, R. C., Grimes, J. P., & Davidsen, A. F. 1997, *ApJ*, 475, 469